

Relativistic N-body simulations with massive neutrinos

Julian Adamek,^a Ruth Durrer^b and Martin Kunz^b

^aLaboratoire Univers et Théories, Observatoire de Paris – PSL Research University – CNRS – Université Paris Diderot – Sorbonne Paris Cité, 5 Place Jules Janssen, 92195 Meudon CEDEX, France

^bDépartement de Physique Théorique & Center for Astroparticle Physics, Université de Genève, 24 Quai E. Ansermet, 1211 Genève 4, Switzerland

E-mail: julian.adamek@obspm.fr, ruth.durrer@unige.ch, martin.kunz@unige.ch

Abstract. Some of the dark matter in the Universe is made up of massive neutrinos. Their impact on the formation of large scale structure can be used to determine their absolute mass scale from cosmology, but to this end accurate numerical simulations have to be developed. Due to their relativistic nature, neutrinos pose additional challenges when one tries to include them in N-body simulations that are traditionally based on Newtonian physics. Here we present the first numerical study of massive neutrinos that uses a fully relativistic approach. Our N-body code, *gevolution*, is based on a weak-field formulation of general relativity that naturally provides a self-consistent framework for relativistic particle species. This allows us to model neutrinos from first principles, without invoking any ad-hoc recipes. Our simulation suite comprises some of the largest neutrino simulations performed to date. We study the effect of massive neutrinos on the nonlinear power spectra and the halo mass function, focusing on the interesting mass range between 0.06 eV and 0.3 eV and including a case for an inverted mass hierarchy.

Contents

1	Introduction	1
2	Numerical approach	2
2.1	Weak-field expansion of the metric	2
2.2	Canonical momentum and geodesic equation	4
2.3	Non-cold dark matter – N-body versus Boltzmann hierarchy	5
2.4	Initial conditions	5
3	Relation to Newtonian simulations	8
4	Description of numerical simulations	11
5	Total matter and neutrino power spectra	13
6	Power spectra of relativistic potentials	17
6.1	Scalar potentials	17
6.2	Vector potential	20
6.3	Tensor perturbations	22
7	Halo mass function	22
8	Conclusion	24
A	Leapfrog integrator for relativistic particles	26
B	Second-order contributions to the relativistic potentials	28

1 Introduction

Since the discovery of the Higgs particle at the LHC [1, 2] the standard model of particle physics is formally complete, except for the still unknown physical origin of the neutrino masses. Neutrino mass differences have been measured through neutrino oscillation experiments (e.g. [3–9]), which indicate squared mass differences of $\Delta m_{21}^2 = (7.37 \pm 0.18) \times 10^{-5} \text{ eV}^2$ and $|\Delta m^2| = (2.50 \pm 0.05) \times 10^{-3} \text{ eV}^2$ (for details and the definition of Δm^2 see section 14 of [10]). But the absolute neutrino mass scale is still unknown, and its determination may provide important clues to the last remaining gap in the standard model of particle physics.

In addition, massive neutrinos impact structure formation in the Universe, e.g. [11]. At early times neutrinos are relativistic and contribute to the radiation density. As the Universe expands, massive neutrinos become non-relativistic and contribute to the total dark matter. But due to their initially high velocities they free-stream out of over-densities and thus reduce the clustering of the dark matter, relative to the standard Λ -cold-dark-matter (Λ CDM) model with massless neutrinos. This impact of neutrino masses on the galaxy clustering in the Universe offers upcoming large galaxy and weak lensing surveys like DESI [12], Euclid [13, 14], LSST [15, 16] or SKA [17] the opportunity to determine the absolute neutrino mass scale with cosmological observations. The *Planck* measurement of the cosmic

microwave background alone already limits the sum of neutrino masses to $\sum m_\nu < 0.49$ eV at 95% confidence level [18]. Adding external data, mainly baryon acoustic oscillations, results in $\sum m_\nu < 0.23$ eV, and the most stringent cosmological constraint, using the Ly- α forest, is $\sum m_\nu < 0.14$ eV at 95% [19]. Current laboratory limits from measurements of the β -decay kinematics are about an order of magnitude higher, see [10], and will reach a sensitivity comparable to the *Planck* constraints only with the KATRIN experiment (e.g. [20]).

However, in order to use cosmology to measure the neutrino masses we have to be able to predict their impact on clustering to high accuracy on a wide range of scales, including those where perturbation theory no longer applies. Mistakes in the predictions will not only bias a measurement of the neutrino masses but generally induce a large systematic error in the results of those surveys, which would compromise the goals of precision cosmology. For this reason we have to rely at least partially on numerical simulations of galaxy clustering including massive neutrinos, as there is no other way to study the evolution of perturbations on strongly non-linear scales. But while cold dark matter (CDM) lives on an effectively three-dimensional sheet in the six-dimensional phase space due to its small velocity dispersion, the relativistic neutrinos fill the full six-dimensional volume, hugely reducing the particle density in phase space and thus increasing the shot noise in any quantity derived from the simulations. An additional problem, particularly for Newtonian simulations, stems from the high initial momenta that require either a relativistic treatment or else lead to superluminal propagation speeds for the neutrinos.

In this paper we discuss simulations of cosmological structure formation including massive neutrinos with the relativistic N-body code *gevolution* [21]. We start with a description of the numerical implementation and the differences to Newtonian simulations of structure formation with neutrinos in Sections 2 and 3. We present our simulation suite in Section 4 and discuss results on the matter power spectrum in Section 5. We study relativistic spectra that are not available in Newtonian simulations in Section 6 and the halo mass function in Section 7. Section 8 summarizes our conclusions. In Appendix A we briefly discuss how to implement a symplectic leapfrog integrator for relativistic particles. Some convolution integrals for second-order source terms of the metric perturbations are collected in Appendix B.

2 Numerical approach

In this section we discuss the key elements of our relativistic N-body code *gevolution*, with particular emphasis on the features relevant for simulating relativistic species. These features are available with the latest public release of the code, which can be obtained at <https://github.com/gevolution-code/gevolution-1.1.git>. While aiming for a self-contained presentation, we refer the reader to [22–24] for additional details.

2.1 Weak-field expansion of the metric

The relativistic framework employed in *gevolution* is based on a geometric interpretation of gravity. The gravitational fields, sourced by the stress-energy tensor, act through a deformation of spacetime that modifies geodesic motion. This has to be contrasted to the Newtonian picture of a two-body force. On cosmological scales the gravitational fields are extremely weak, as can be seen easily by considering e.g. the compactness parameter of the structure at those scales: galaxies and clusters have a typical size many orders of magnitude larger than their Schwarzschild radius. We can therefore choose an appropriate ansatz for the perturbed metric and perform a systematic expansion of Einstein’s field equations in terms of the weak

gravitational fields. However, it is important to pick a coordinate system in which the geometry indeed remains weakly perturbed, and some of the simple coordinate choices can fail miserably. We employ the coordinate system of the Poisson gauge that has proven to be very well adapted to this requirement (see also [25]). The line element reads

$$ds^2 = g_{\mu\nu} dx^\mu dx^\nu = a^2(\tau) \left[-e^{2\psi} d\tau^2 - 2B_i dx^i d\tau + \left(e^{-2\phi} \delta_{ij} + h_{ij} \right) dx^i dx^j \right], \quad (2.1)$$

where τ is conformal time, x^i are coordinates on the spacelike hypersurface, and ψ , ϕ , B_i , h_{ij} are the gravitational fields that characterize the deformation of the geometry away from a Friedmann-Lemaître model. The coordinate system is fixed by the gauge conditions

$$\delta^{ij} B_{i,j} = \delta^{ij} h_{ij} = \delta^{jk} h_{ij,k} = 0, \quad (2.2)$$

where we introduced the shorthand $f_{,i} \doteq \partial f / \partial x^i$. We will also use $f' \doteq \partial f / \partial \tau$ and $\Delta f \doteq \delta^{ij} f_{,ij}$, as well as $\mathcal{H} \doteq a' / a$.

Note that the two scalar potentials ϕ and ψ are introduced in a slightly different way than the corresponding potentials Φ and Ψ used in the original version of *gevolution* [23]. This change of convention pays tribute to the fact that $(\phi - \psi)$ has an improved behaviour at second order compared to $(\Phi - \Psi)$ [24]. At first order the two definitions are equivalent, and we will continue using the symbol $\chi \doteq \phi - \psi$ which is now defined with respect to the new convention.

In the linear evolution of standard cosmology the vector mode B_i has no source, it decays and is usually discarded. The spin-2 field h_{ij} and the gravitational slip χ can only be sourced by relativistic species at first order, and hence they also decay inside the horizon once radiation domination comes to an end some 100 000 years after the Big Bang. Therefore, except for the case of a large contribution of primordial gravitational waves, the second-order contributions to h_{ij} and χ eventually dominate at (sufficiently large) sub-horizon scales. A consistent computation of these contributions includes some quadratic terms constructed from the first-order perturbations ψ and ϕ . Apart from these terms, which are only relevant in the regime where stress-energy perturbations are small (otherwise these quadratic weak-field terms cannot compete with the stress-energy and are subdominant), it is sufficient to truncate the weak-field expansion at leading order. Einstein's field equations can then be written as

$$(1 + 2\phi) \Delta\phi - 3\mathcal{H}\phi' - 3\mathcal{H}^2 (\phi - \chi) - \frac{1}{2} \delta^{ij} \phi_{,i} \phi_{,j} = -4\pi G a^2 \delta T_0^0, \quad (2.3)$$

$$\Delta^2 B_i = 16\pi G a^2 P_i^j T_j^0, \quad (2.4)$$

$$\Delta^2 \chi - \left(3\delta^{ik} \delta^{jl} \frac{\partial^2}{\partial x^k \partial x^l} - \delta^{ij} \Delta \right) \phi_{,i} \phi_{,j} = 4\pi G a^2 \left(3\delta^{ik} \frac{\partial^2}{\partial x^j \partial x^k} - \delta_j^i \Delta \right) T_i^j, \quad (2.5)$$

$$\Delta^2 (h_{ij}'' + 2\mathcal{H}h_{ij}' - \Delta h_{ij}) - 4 \left(P_i^k P_j^l - \frac{1}{2} P_{ij} P^{kl} \right) \phi_{,k} \phi_{,l} = 16\pi G a^2 \left(P_{ik} P_j^l - \frac{1}{2} P_{ij} P_k^l \right) T_l^k, \quad (2.6)$$

where we define the transverse projection operator as

$$P_{ij} \doteq \frac{\partial^2}{\partial x^i \partial x^j} - \delta_{ij} \Delta. \quad (2.7)$$

Three additional equations are not written here: a scalar equation obtained from the spatial trace, the longitudinal part of the momentum constraint, and the spin-1 projection on the

spatial hypersurface. These are degenerate with the covariant conservation of stress-energy which also amounts to two scalar and one spin-1 equations, but one can use them to check this conservation law within the numerical scheme. Furthermore, we have subtracted a background contribution from the Hamiltonian constraint, given by the Friedmann equation

$$\frac{3}{2}\mathcal{H}^2 = -4\pi G a^2 \bar{T}_0^0. \quad (2.8)$$

It is often assumed that this subtraction ensures that the remaining perturbations have zero average, but it turns out that this is a nontrivial requirement that is not automatically fulfilled beyond leading order. Instead of imposing this condition, it is however sufficient to subtract an approximate background model, i.e. a contribution that allows for a finite residual that is however perturbatively small. In practice we use a reference Friedmann model for the given cosmology and subtract exactly the same quantity on either side of the equation, hence defining $\delta T_0^0 \doteq T_0^0 - \bar{T}_0^0$ without assuming an exactly vanishing average for δT_0^0 . Consistency of the equations is dynamically maintained by allowing for a homogeneous mode in ϕ and ψ . The scheme remains valid as long as this homogeneous mode remains sufficiently small.

The stress-energy for the particle ensemble is computed non-perturbatively, however, on the weakly perturbed geometry. This means that the quantities obtained from the particle-mesh projection are dressed by linear geometric corrections that describe, for instance, the perturbation of the volume element.

2.2 Canonical momentum and geodesic equation

Adhering to its general relativistic approach *gevolution* uses a canonical momentum q_i , rather than a peculiar velocity, in order to describe phase space. The advantage of this description is that it remains valid for arbitrarily large momenta, including in particular the ultra-relativistic limit $q^2 \gg m^2 a^2$, where m is the proper rest-mass. The geodesic equation reads

$$q'_i = -\frac{2q^2 + m^2 a^2}{\sqrt{q^2 + m^2 a^2}} \phi_{,i} + \sqrt{q^2 + m^2 a^2} \chi_{,i} - q^j B_{j,i} + \frac{1}{2} \frac{q^j q^k h_{jk,i}}{\sqrt{q^2 + m^2 a^2}}. \quad (2.9)$$

The first two terms are the usual gravitational deflection, featuring the correct ultra-relativistic limit relevant for weak lensing. The third term incorporates frame-dragging which is already a very small effect under most realistic circumstances. The last term describes the scattering of particles on gravitational waves. This interaction is so weak that it certainly cannot affect structure formation unless one constructs very exotic scenarios. Therefore, to reduce computational cost, this term is currently neglected in *gevolution* even though it would be straightforward to include it. Frame-dragging, however, is taken into account.

The coordinate three-velocity is related to q_i as

$$\delta_{ij} \frac{\partial x^j}{\partial \tau} = \frac{q_i}{\sqrt{q^2 + m^2 a^2}} \left[1 + \left(3 - \frac{q^2}{q^2 + m^2 a^2} \right) \phi - \chi + \frac{1}{2} \frac{q^j q^k h_{jk}}{q^2 + m^2 a^2} \right] + B_i - \frac{h_{ij} q^j}{\sqrt{q^2 + m^2 a^2}}, \quad (2.10)$$

where, as above, we may choose to neglect the terms involving h_{ij} . The last two equations are directly implemented in the staggered leapfrog integrator for the particle evolution. Some theoretical aspects of this integrator are discussed in Appendix A.

2.3 Non-cold dark matter – N-body versus Boltzmann hierarchy

Following the terminology used in *CLASS* [26] we will call any relativistic species that can be modelled as collisionless massive particles a non-cold dark matter (NCDM) component, of which massive neutrinos in the late Universe are just one particular realization. The lack of a scattering process means that such a NCDM component is not driven towards an equilibrium and therefore develops a complex phase-space structure that cannot be mapped to a fluid description even at first order. In the linear Boltzmann approach such a component is modelled by taking into account a large number of multipoles in the distribution function and solving their coupled evolution [27]. If high accuracy is required this can easily involve hundreds of coupled equations. The fundamental limitation of this approach is the assumed linearity: non-linear clustering of NCDM cannot be taken into account easily.

The alternative is to directly use the N-body scheme as a Monte Carlo method to sample the phase space of NCDM. While conceptually straightforward there are practical limitations on the number of samples one can draw in a simulation, typically leading to very noisy representations. Relativistic species have a very broad momentum distribution – this is exactly what distinguishes NCDM from CDM. One then has to be very careful that the shot noise from sampling does not produce spurious clustering in the simulation. This issue is greatly alleviated for simulations of massive neutrinos in the context of Λ CDM since in this case the NCDM makes up only a small fraction of the dark matter. It is therefore possible to reduce the NCDM shot noise well below the perturbation amplitude of CDM, at which point it causes no harm anymore. Note that this would not apply in situations where none of the dark matter is cold, like e.g. in warm dark matter models.

We thus have two entirely different approaches at our disposal (see Figure 1 for an illustration) – the Boltzmann approach that works in Fourier space and gives very accurate results that are however confined to the linear regime, and the N-body approach that can follow the evolution in configuration space nonperturbatively but has to deal with shot noise. Several attempts have been made to combine or extend these two approaches [28–31]. In this work we employ the N-body approach, i.e. a separate N-body ensemble is simulated for each NCDM species. However, it is also possible to link *CLASS* to *gevolution*, thus allowing the code to compute any linear transfer function by calling *CLASS* at runtime. One can then choose whether one wants to use the linear realization of the perturbations as given by the Boltzmann solution (as was advocated in [28]), or the noisy but nonperturbative realization of the perturbations as given by the N-body ensemble, as input for the stress-energy tensor which is used for solving the metric. The choice can be made separately for each species, and in *gevolution* the user can specify redshift values at which the code switches between the two methods. This can be useful because the noise is of increasing concern at higher redshift when the CDM perturbations are still rather small and the NCDM particles have large velocities. At the same time the perturbations are still linear to good approximation and the Boltzmann approach is well justified.

2.4 Initial conditions

Setting initial conditions for N-body simulations with neutrinos has been considered somewhat of an art. This has a lot to do with the fact that Newtonian codes have to be repurposed for a task to which they are not very well adapted [32]. With *gevolution* the story is quite different: its underlying relativistic framework allows an implementation that is conceptually clean and straightforward, based on a procedure outlined in [33].

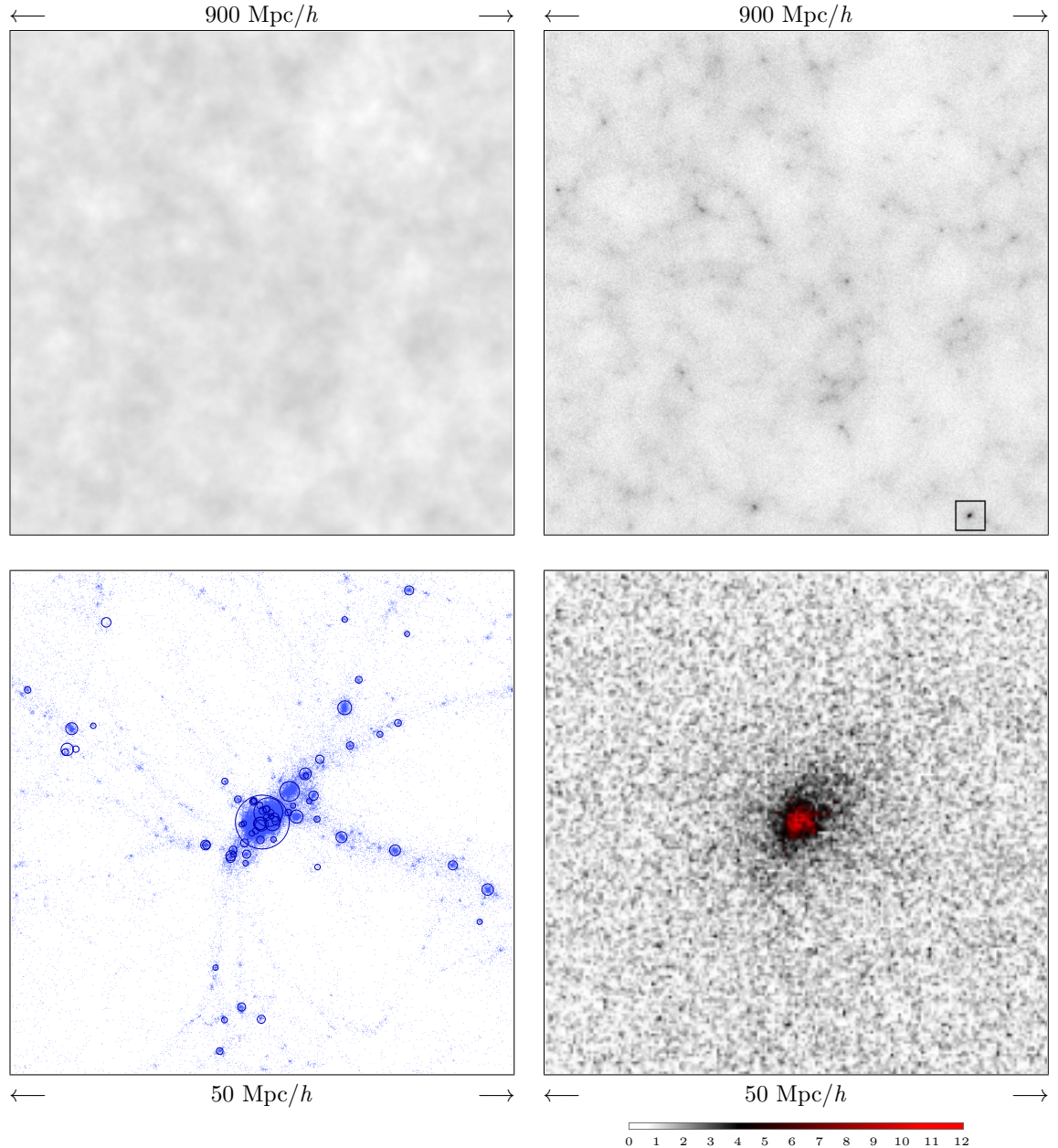


Figure 1. Slice through a simulation with massive neutrinos ($\sum m_\nu = 0.2$ eV) at redshift $z = 0$. The upper panels show the neutrino density field across the entire simulation box, projected along the 5 Mpc/h thickness of the slice. The upper left shows the result obtained using the linear realization of the density field constructed from the transfer functions that were computed by *CLASS*. The upper right shows the same realization using the N-body method. While being somewhat noisy, the N-body method is able to follow the nonlinear evolution of the neutrino distribution. The lower right panel is a zoom into a region containing a massive structure, showing that the density contrast $\delta_\nu = \delta\rho_\nu/\bar{\rho}_\nu$ of the neutrino component can be larger than unity (scale bar indicates $\delta_\nu + 1$). To provide some context, the CDM distribution for the same region is shown in the lower left panel, with circles indicating the locations and virial radii of friends-of-friends halos detected with the *ROCKSTAR* halo finder [34]. Note that the particle snapshots used for this figure were downgraded by a factor of 32 to make the files more easy to handle; the actual simulation therefore had a much lower noise level.

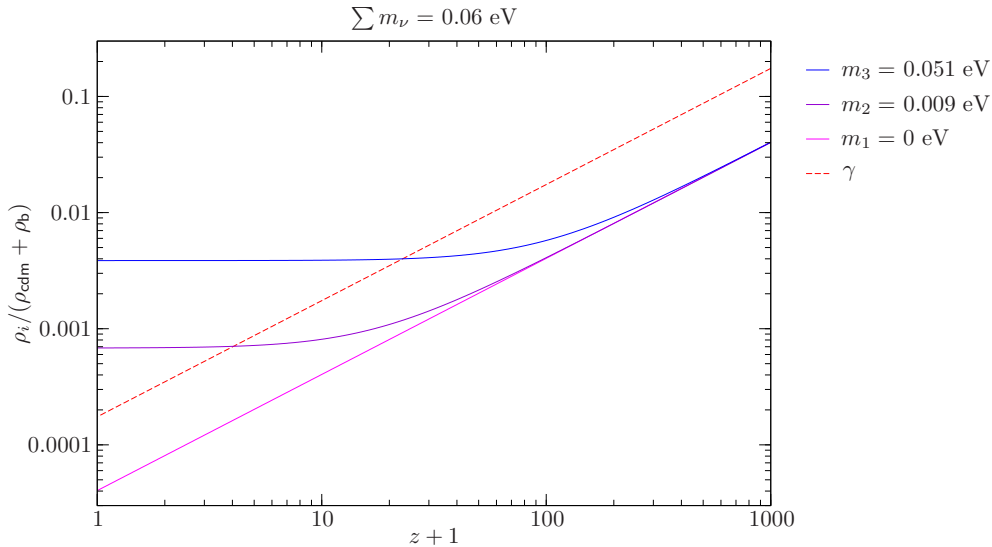


Figure 2. Evolution of the energy density of photons (dashed line) and the three neutrino species in a minimal mass scenario, relative to the energy density of the remaining matter (CDM and baryons).

We initialize the neutrino N-body ensembles at a redshift where the particle horizon is of the order of the spatial resolution of the simulation, such that all modes are initially outside the horizon. For our values of the resolution this typically requires a redshift well above 10^5 . At this time the perturbations are still adiabatic and Gaussian. Furthermore, the phase-space distribution function is still close to the initial Fermi-Dirac distribution produced by thermal freeze-out. The initial neutrino momenta are drawn from this initial distribution using a fast rejection-sampling method, including the temperature monopole and dipole perturbations caused by density and velocity perturbations of the primordial plasma. The higher moments of the distribution function are negligible far outside the horizon and only build up over time.

The free-streaming neutrino particles are then evolved down to a much lower redshift where baryons and CDM will be added. In all our simulations this happens at $z_{\text{ini}} \simeq 127$. Following [33] we evolve the neutrinos in the linearly perturbed metric, where we obtain the relevant transfer functions of ϕ and ψ by calling *CLASS* at runtime. This procedure is in some sense equivalent to solving the full Boltzmann hierarchy for the neutrino phase space. At z_{ini} we set up the N-body ensemble of CDM and baryons, represented as a single species with perturbations given as weighted averages of the linear CDM and baryon density and velocity transfer functions. All the baryonic physics happening before photon decoupling is hence taken into account in these initial conditions. As shown in Figure 2 the relativistic energy density of each neutrino species has also dropped to $\lesssim 1\%$ of the CDM density at that redshift, allowing the effect of shot noise to be kept under control.

From this point onward the metric is solved using the N-body ensembles and the simulation eventually proceeds into the nonperturbative regime. The perturbations of photons, which account for a waning percentage of the total energy density of the Universe, are neglected and we only keep their contribution to the background. The same is done for any massless neutrino states. Inside the horizon the perturbations of these radiation components decay and can no longer compete with the growing matter perturbations. Close to the hori-

zon, on the other hand, their perturbations can still have a subtle effect reaching deep into the matter dominated era [24, 35]. This effect can be taken into account in *gevolution*, again by constructing the linear perturbations according to transfer functions obtained through *CLASS*. Details on this procedure are given in [24], but after running some tests we convinced ourselves that we do not need to include it in our production runs with a box size of $2 \text{ Gpc}/h$ and less.

3 Relation to Newtonian simulations

N-body simulations with massive neutrinos have so far mostly been carried out using Newtonian codes. We therefore want to discuss how results should be compared between the different approaches. One challenging aspect is the fact that space and time are absolute concepts in Newton’s theory. This poses the problem of identifying the foliation of spacetime that best corresponds to the Newtonian picture. The Newtonian gauge, which is just another name for the scalar sector of the Poisson gauge, seems to be a good choice on scales much smaller than the horizon. In this limit eq. (2.3) becomes

$$\Delta\phi = 4\pi G a^2 \delta\rho, \quad (3.1)$$

keeping the leading weak-field order only since the next order is already post-Newtonian. The Newtonian approximation is only valid if all gravitating matter moves at small velocities such that kinetic energy can always be neglected against rest mass energy. Massive neutrinos fulfill this criterion only to a limited extent, and for the comparison discussed below we will choose neutrino masses such that kinetic energy is subdominant within the redshift interval covered by the N-body simulation. In the nonrelativistic limit $q^2 \ll m^2 a^2$ the geodesic equation (2.9) reduces to

$$q'_i = -m a \phi_{,i}, \quad (3.2)$$

where we used $\chi = 0$ as a result of the Newtonian approximation. With eq. (2.10) the peculiar velocity is simply

$$\delta_{ij} \frac{\partial x^j}{\partial \tau} = \frac{q_i}{m a} \quad (3.3)$$

at leading order. Eqs. (3.1)–(3.3) of course are exactly the equations of Newtonian gravity with ϕ playing the role of the Newtonian potential.

The direct link between Newtonian gravity and the Newtonian gauge does unfortunately not persist on very large scales. As one approaches the cosmological horizon, terms like $\mathcal{H}^2 \phi$ become important in the Hamiltonian constraint (2.3) such that eq. (3.1) is no longer a useful truncation. This issue led to an interesting debate on how one should interpret Newtonian simulations at those scales [36–40]. For linear scales the problem has finally been solved in [38, 41, 42] by realizing that there exists a class of gauges that is compatible with Newtonian dynamics by construction. While this allows one to obtain a relativistic interpretation of the two-point function of Newtonian simulations at very large separations, many aspects still remain to be worked out. For instance, it is not obvious how the analysis of weak gravitational lensing would have to be adjusted.

For the purpose of our comparison we will make use of the so-called N-body gauge, introduced in [41]. This gauge, defined in the linear regime, has the property that the equations reduce to the Newtonian ones on arbitrary scales if all sources of perturbations are

non-relativistic. This approximation is excellent for CDM and baryons and works still fairly well for massive neutrinos as soon as they are sufficiently cold.

In order to allow for a comparison that is minimally affected by aspects of implementation we employ the Newtonian mode of *gevolution* to run Newtonian simulations. In this case the code first prepares the initial conditions in exactly the same way as it is done for relativistic runs, explained in Section 2.4, and then applies an additional step: from the linear transfer functions provided by *CLASS* the code computes the gauge transformation between Poisson and N-body gauge, i.e. two scalar potentials whose gradients are the displacement and velocity correction describing the active coordinate transformation that has to be applied to the N-body ensemble. After the initial data has thereby been put into N-body gauge the simulation is performed using the Newtonian equations (3.1)–(3.3).

It is worth noting that the neutrino particles in the tail of the distribution move at superluminal velocity under this prescription, as the thermal velocity is assumed to redshift as $1/a$ at all times without accounting for the Lorentz factor. This issue, mainly relevant at high redshift, has so far been treated as an acceptable limitation of Newtonian simulations. Concerned by the apparent loss of causality, in [23] we advocated to restore Lorentz invariance by replacing equations (3.2) and (3.3) by

$$q'_i = -\frac{2q^2 + m^2a^2}{\sqrt{q^2 + m^2a^2}}\phi_{,i}, \quad (3.4)$$

and

$$\delta_{ij}\frac{\partial x^j}{\partial\tau} = \frac{q_i}{\sqrt{q^2 + m^2a^2}}, \quad (3.5)$$

respectively, without modifying the computation of ϕ . The latter is probably justified because the relativistic tail of the neutrino distribution only gives a tiny contribution to the total gravitational field which is dominated by CDM and baryons. It should be straightforward to implement the above equations of motion in any Newtonian code, and we will call the resulting scheme “Newtonian gravity with special relativity”.

We therefore have three different simulation types to compare, corresponding to three different levels of approximation. The least accurate one, which at the same time is the one widely used in the literature, is Newtonian gravity with Newtonian mechanics. The second one, aiming at a rectification of the evolution of relativistic test particles, is Newtonian gravity with special relativity. The third one, finally, is our general relativistic weak-field framework. For each simulation type we carry out runs for a cosmology with a sum of neutrino masses $\sum m_\nu = 0.2$ eV (more details on the cosmology are given in the next section), with an ensemble of 2048^3 particles for CDM and baryons and about 21 billion neutrino particles. In order to study convergence on small and large scales we use two different box sizes, 2 Gpc/ h and 4 Gpc/ h , giving us a total of six different runs for this study. We also use the same random number sequence to set up the perturbations in each type of simulation in order to suppress effects of realization scatter.

As the Newtonian results should be interpreted in N-body gauge, we choose this gauge for our comparison. The runs performed with the general relativistic approach use Poisson gauge in the simulation, however, at the time the output is written we apply the appropriate active coordinate transformation to convert the results into N-body gauge. This is done exactly in the same way as it was done for the initial data of the Newtonian runs, only that this time it is done at the end of the run and not at the beginning. Since the transformation is computed

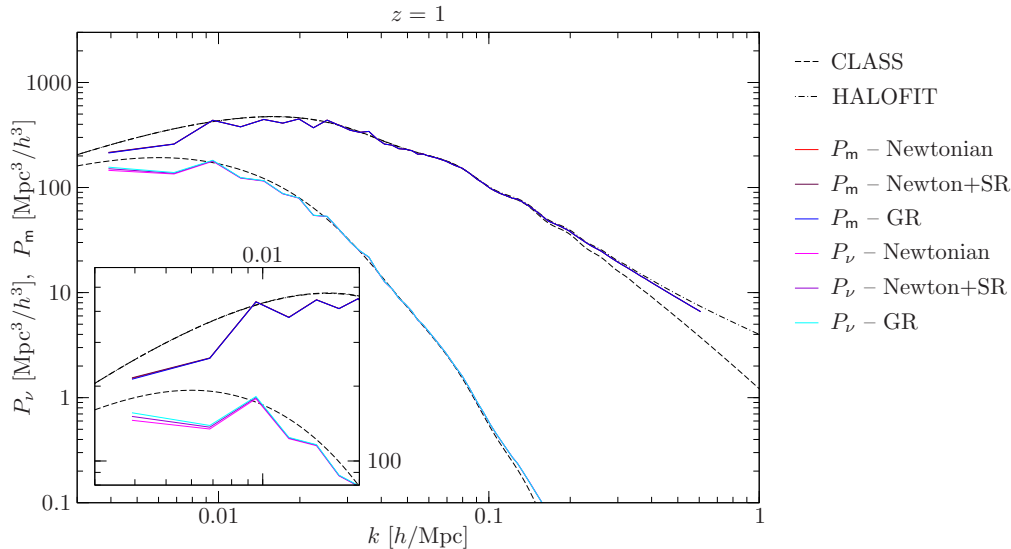


Figure 3. We show the total matter power spectrum (top curves) and neutrino power spectrum (lower curves) in N-body gauge at redshift $z = 1$ for three different simulation modes, together with the linear predictions from *CLASS* and the nonlinear HALOFIT model. The sum of neutrino masses was chosen as $\sum m_\nu = 0.2$ eV for this study. We compare results from a Newtonian run, a run with Newtonian gravity and special relativity (SR), and a run using our general relativistic (GR) framework (see text for details). The inset magnifies the large-scale portion of the spectra where differences in the three simulation modes start to show up. All runs used the same initial conditions, with a simulation box of $2 \text{ Gpc}/h$, 2048^3 particles for CDM and baryons, and about 2.1×10^{10} neutrino particles.

within linear theory one may be worried that there could be a problem at nonlinear scales; however, the coordinate change goes to zero on those scales, simply because the Poisson gauge assumes the Newtonian limit discussed at the beginning of this section.

Despite the various approximations it turns out that the results agree remarkably well between the three methods. As shown in Figure 3 the nonlinear total matter and neutrino power spectra are practically indistinguishable at small scales. At very large scales a small disagreement (somewhat less than one per cent on the total matter power at $k \sim 0.005 \text{ h}/\text{Mpc}$) appears whose amplitude seems compatible with the expected error induced by neglecting neutrino anisotropic stress in the Newtonian simulations [24]. As we will show in Section 6 this effect is fully taken into account in our relativistic runs. The same is true also for the kinetic energy of the neutrinos which may also give rise to some corrections at high redshift. A possible way to deal with both effects would be to use the “Newtonian motion gauge” framework introduced in [42], but for the case of massive neutrinos this still requires some development. In addition, we expect a small error on the effective free-streaming length of neutrinos when using Newtonian mechanics, which could explain some of the effect we see in the neutrino power spectrum at large scales. In the end it is hard to disentangle all these contributions in our results.

One other aspect is worth pointing out. When we integrate the particle equations (see Appendix A) we choose the time step by requiring that the particles are allowed to move only a certain maximum distance in each leapfrog step. For CDM particles the global time

L_{box}	resolution	$N_{\text{cdm+b}}$	N_ν	m_1	m_2	m_3	$\sum m_\nu$
2 Gpc/h	0.5 Mpc/h	4096 ³	—	0 eV	0 eV	0 eV	0 eV
2 Gpc/h	0.5 Mpc/h	4096 ³	1.7×10^{11}	0 eV	0.009 eV	0.051 eV	0.06 eV
2 Gpc/h	0.5 Mpc/h	4096 ³	1.7×10^{11}	0.0225 eV	0.0225 eV	0.055 eV	0.1 eV
2 Gpc/h	0.5 Mpc/h	4096 ³	1.7×10^{11}	0.05 eV	0.05 eV	0 eV	0.1 eV
2 Gpc/h	0.5 Mpc/h	4096 ³	1.7×10^{11}	0.06 eV	0.06 eV	0.08 eV	0.2 eV
2 Gpc/h	0.5 Mpc/h	4096 ³	1.7×10^{11}	0.1 eV	0.1 eV	0.1 eV	0.3 eV
0.9 Gpc/h	0.25 Mpc/h	3600 ³	—	0 eV	0 eV	0 eV	0 eV
0.9 Gpc/h	0.25 Mpc/h	3600 ³	1.2×10^{11}	0.06 eV	0.06 eV	0.08 eV	0.2 eV
8 Gpc/h	2.0 Mpc/h	4096 ³	—	0 eV	0 eV	0 eV	0 eV
8 Gpc/h	2.0 Mpc/h	4096 ³	1.7×10^{11}	0.06 eV	0.06 eV	0.08 eV	0.2 eV

Table 1. Main characteristics of our production runs. These simulations used a total of 2.2 million CPU-hours on the Cray XC50 *Piz Daint* at the Swiss National Supercomputing Centre.

step (used in the gravity solvers) ensures that this maximum distance is below one grid unit, but for the neutrino particles we may have to choose smaller time steps – in fact, we even allow some portion in the tail of the distribution to travel by more than one grid unit. Applying the same maximum distance criterion in all simulations, the ones with Newtonian mechanics end up needing many more time steps for integrating the neutrino equations due to the aforementioned issue of superluminal velocities. These simulations therefore consume significantly more computational resources than the ones with special relativity, even though equations (3.4) and (3.5) contain additional operations. We therefore conclude that the use of the special relativistic equations not only restores causality but also may prove more economic for simulations that employ a time step criterion based on particle velocities. However, the common practice so far has been to use a time step criterion that is independent of the neutrino velocity, thus allowing the neutrinos to move by an arbitrary distance in each step.

4 Description of numerical simulations

For the remainder of the paper we discuss results from a large suite of N-body simulations carried out with *gevolution*. This is the first time that such a comprehensive numerical study is based entirely on a relativistic approach. As summarized in Table 1 we explore the mass range between $\sum m_\nu = 0.3$ eV and the minimal mass scenario, $\sum m_\nu = 0.06$ eV, and also include a case where we can compare a normal mass hierarchy ($m_1 \lesssim m_2 < m_3$) to an inverted one ($m_3 < m_1 \lesssim m_2$) at fixed total mass $\sum m_\nu = 0.1$ eV. Except for the minimal mass scenario we neglect the smaller Δm_{21}^2 mass splitting, therefore running with no more than two distinct mass eigenstates. We choose a relatively large simulation volume with a box size of $L_{\text{box}} = 2$ Gpc/h in order to have good statistics at nonlinear scales. This also ensures that two important scales are contained in our dynamical range: the equality scale at ~ 0.4 Gpc/h which characterizes the peak of the matter power spectrum, and the neutrino free-streaming length which (depending on mass) is typically around 1.5 Gpc/h. These simulations have a spatial resolution of 0.5 Mpc/h and contain 4096³ particles for the CDM and baryonic component, corresponding to a mass resolution of roughly $10^{10} M_\odot/h$.

The neutrino components are simulated using N-body ensembles with a total of 1.7×10^{11} tracers which are evolved as if they were fundamental particles of the species they represent. These tracers sample the neutrino phase space and are used to construct a Monte Carlo

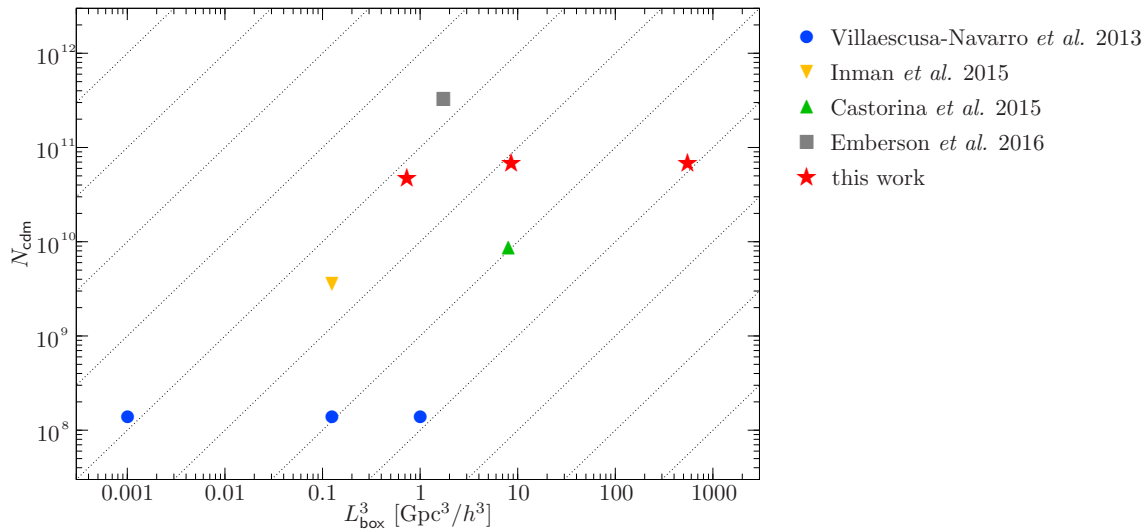


Figure 4. Diagrammatic comparison of our production runs with some recent N-body simulations carried out by other groups [43–46] to study massive neutrinos. The dotted lines show the lines of constant mass resolution in the CDM component. The number of neutrino particles per CDM particle varies between $N_\nu/N_{\text{cdm}} = 1$ and $N_\nu/N_{\text{cdm}} = 8$; we run at $N_\nu/N_{\text{cdm}} = 2.5$.

representation of the neutrino stress-energy tensor. Since the number of tracers is much smaller than the true number of fundamental particles, the total stress-energy is obtained by multiplying the one of the tracers by a corresponding large factor. This makes sense since the stress-energy is an extensive quantity and the ensemble of tracers represents a fair sample. In the cases where several different mass eigenstates are simulated, the size of the sub-ensembles for the different masses is chosen such that in the nonrelativistic limit each tracer has the same fractional contribution to the stress-energy. This also means that massless states are not represented as an N-body ensemble – they are included in the background radiation density but their perturbations are neglected. This is justified since radiation perturbations decay inside the horizon.

In order to study finite-volume as well as resolution effects, we carry out two pairs of additional production runs. One has a larger box of $L_{\text{box}} = 8 \text{ Gpc}/h$ and hence significantly more volume but lower resolution, the other one has a smaller box of $L_{\text{box}} = 0.9 \text{ Gpc}/h$ with a resolution of $0.25 \text{ Mpc}/h$. At given L_{box} all simulations use exactly the same random number sequence to set up the initial perturbations. Therefore, if we take ratios of numerical power spectra, the cosmic variance will cancel on linear scales. In order to test various systematics we additionally run over 30 smaller simulations like the ones discussed in Section 3.

The following values of cosmological parameters are common to all simulations: $A_s = 2.215 \times 10^{-9}$ (at $k_{\text{pivot}} = 0.05 \text{ Mpc}^{-1}$), $n_s = 0.9619$, $h = 0.67556$, $\omega_b = 0.022032$, $T_{\text{cmb}} = 2.7255 \text{ K}$, $N_{\text{eff}} = 3.046$ (in the ultrarelativistic limit) and no spatial curvature. We want to maintain a fixed total matter density and hence set $\omega_{\text{cdm}} = 0.12038 - \sum m_\nu / (93.14 \text{ eV})$ according to the neutrino mass contribution. We assume the standard scenario of neutrino freeze-out to set the initial parameters of the neutrino distribution function.

Figure 4 shows a diagram comparing large N-body simulations with massive neutrinos

carried out over the past five years. The studies [43, 45] use a modified version of the code *Gadget* [47], whereas [44, 46] use the code *CUBEP³M* [48]. Both are Newtonian N-body codes based on hybrid implementations that combine a particle-mesh approach on large scales with a direct particle-particle interaction on small scales. Our code currently lacks the latter feature and is hence less suited for analyzing the detailed evolution of small structures. On the other hand, for the first time we are able to perform a self-consistent ab initio simulation including all relativistic effects. The regular lattice used for the particle-mesh algorithm in *gevolution* also allows for a very efficient parallelization that can be scaled up to very large problem sizes. A typical production run with massive neutrinos (see Table 1) parallelized over 16384 CPUs of the Cray XC50 supercomputer *Piz Daint* consumed about 270 000 CPU-hours, approximately corresponding to 16 hours wall clock time. As the diagram in Figure 4 shows, we present in this paper some of the largest neutrino N-body simulations performed to date in terms of particle number, second only to [46] which is however just one single simulation – all other studies ran a suite of simulations to explore various masses.

5 Total matter and neutrino power spectra

Figure 5 shows the total matter power spectra (top panel) and neutrino power spectra (bottom panels) for a series of redshifts for the case $\sum m_\nu = 0.2$ eV. We adopt the usual definition that total matter consists of CDM, baryons and massive neutrinos. The density contrast was computed in Poisson gauge, as this is the gauge that underpins our relativistic framework. Indeed one may notice the characteristic change of slope at scales outside the horizon. As is evident from the neutrino power spectra, sampling the neutrino component with more than 10^{11} particles allows us to obtain a very low level of shot noise and thus to prevent any spurious clustering even at high redshift. Especially at low redshift the signal-to-noise ratio is good enough to see nonlinear effects in the neutrino component alone. At large scales all spectra show good agreement with linear theory (as computed with *CLASS*). In the late Universe nonlinear effects appear at smaller scales.

The shot noise in the neutrino power spectra is due to the auto-correlation of self-pairs and there are different possibilities to eliminate or subtract it [49]. We choose to split each neutrino N-body ensemble randomly into two sub-ensembles and use their cross-correlation as an estimator for the power spectrum like in [44]. This completely eliminates the contribution of the self-pairs. We will later use the same method to suppress shot noise in the power spectrum of χ which linearly depends on the neutrino anisotropic stress, see [23] for more details.

We want to compare our numerical results to the HALOFIT model, a nonlinear recipe commonly used in the literature to model the matter power spectrum. We use the implementation provided by *CLASS* which is based on [50] with improvements from [51] to include the effects of neutrino masses. It is often claimed that Newtonian codes compute the density contrast of synchronous gauge. This belief is based on the fact that the Newtonian density contrast agrees with the one of a synchronous gauge in the linear regime, but unfortunately this is no longer true in the nonlinear case where even the very definition of a synchronous coordinate system faces challenges. In fact, also at linear scales it is conceptually more accurate to say that Newtonian simulations perform computations in the N-body gauge, as discussed in Section 3. The N-body gauge employs the same time slicing as the synchronous gauge which is precisely the reason why the density perturbations match between the two gauges (but other quantities do not, e.g. the coordinate velocity). At nonlinear scales it is less clear

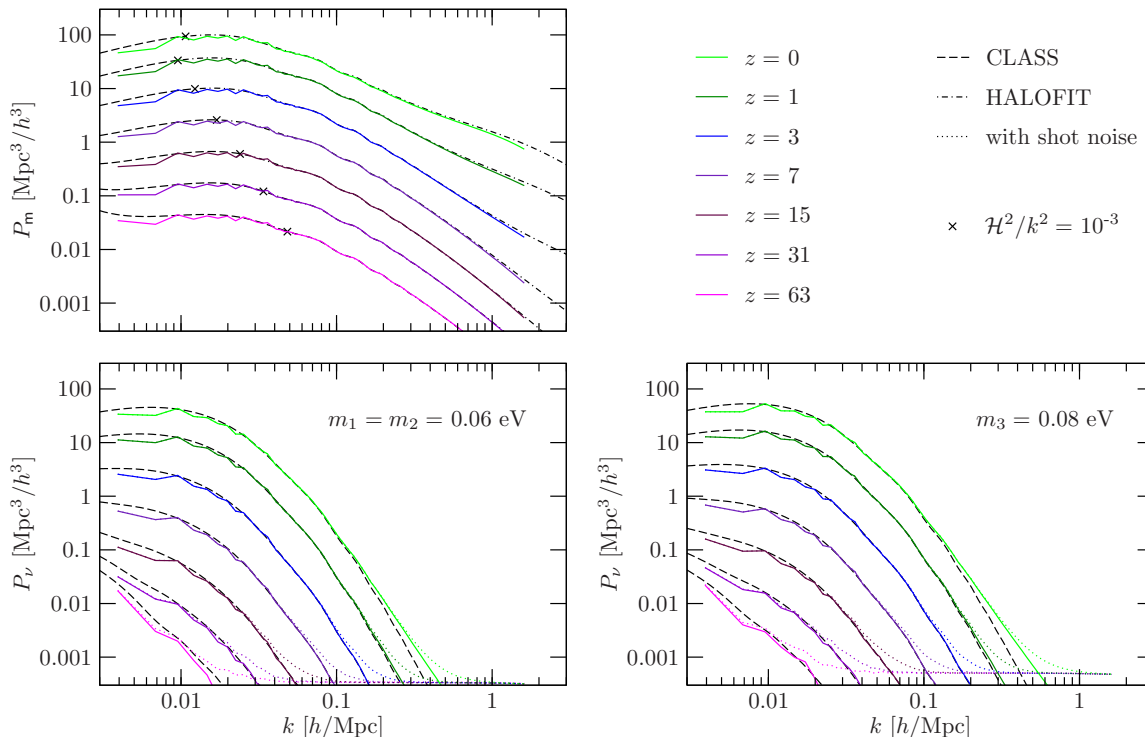


Figure 5. For the case $\sum m_\nu = 0.2$ we show the numerical power spectra in Poisson gauge of total matter, P_m , as well as those of the individual neutrino components, P_ν , evolving over redshifts from $z = 63$ to $z = 0$. The numerical data is from our simulation with $L_{\text{box}} = 2 \text{ Gpc}/h$. For the neutrino components we also show the spectra including the shot noise (dotted lines) in order to highlight the low noise level we can achieve, characterized by the amplitude at which these spectra level off horizontally at the bottom of each panel. The dashed black lines indicate the corresponding linear spectra obtained from *CLASS*, whereas the dash-dotted lines show the HALOFIT model of P_m for nonlinear scales. Since the HALOFIT power spectrum matches to synchronous gauge at linear scales, we only use it deep inside the horizon where gauge effects $\propto \mathcal{H}^2/k^2$ are strongly suppressed. For each curve we mark the point at which \mathcal{H}^2/k^2 reaches 10^{-3} , and at larger scales we again show the linear spectrum in Poisson gauge instead.

which gauge one should associate to a Newtonian simulation, as one would have to extend the concept of the N-body gauge. However, as can be seen from the Newtonian limit discussed in Section 3, the difference to the Poisson gauge is expected to be of order \mathcal{H}^2/k^2 . In Figure 5 we mark the point on each curve where $\mathcal{H}^2/k^2 = 10^{-3}$ and hence the large-scale gauge effects give a permille correction. This point moves towards larger scales at late times and is close to $k \simeq 0.01 \text{ h}/\text{Mpc}$ at redshifts $z \lesssim 3$. We therefore conclude that we can directly compare our results from Poisson gauge to the HALOFIT model, which was calibrated to Newtonian simulations and hence refers to an unspecified gauge that is sufficiently close to Poisson gauge on scales $k \gtrsim 0.01 \text{ h}/\text{Mpc}$ for $z \lesssim 3$.

To get a better impression of the absolute accuracy as well as the robustness with respect to resolution effects, Figure 6 shows the ratios of our numerical matter power spectra with respect to the HALOFIT model at redshift $z = 0$. In addition, we also show the ratios with

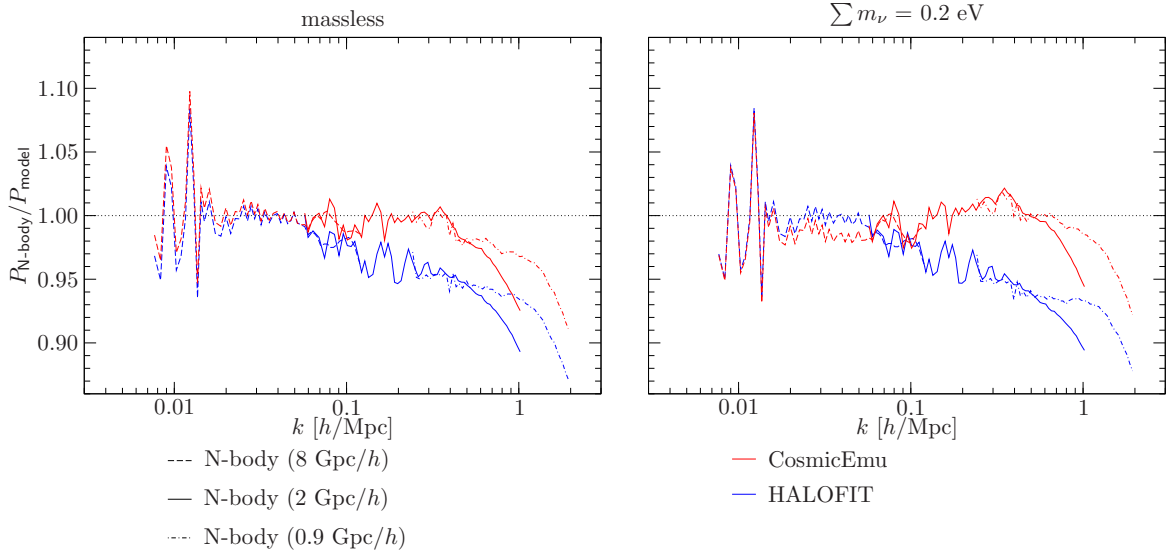


Figure 6. At redshift $z = 0$ we compare our numerical power spectra of total matter to two nonlinear recipes: the HALOFIT model (blue) and the latest revision of the Cosmic Emulator (red). We show the massless case and the case $\sum m_\nu = 0.2 \text{ eV}$ for which we have three different simulations each to cover a larger range of scales and check for resolution effects. In both cases the HALOFIT model systematically predicts too much power (the ratio is below unity), about 5% around the nonlinear scale $k_{\text{nl}} \simeq 0.3 \text{ h/Mpc}$. In the massless case the Cosmic Emulator agrees very well with our results, showing no systematic deviation at all for $k \lesssim k_{\text{nl}}$. The agreement is also quite good for the massive neutrino case, although the emulated power spectrum has a slightly different shape, with more power on large scales and less power on small scales, compared to our numerical result. The disagreement is however well within the 4% error budget of the Cosmic Emulator. The comparison between the 2 Gpc/h and the 0.9 Gpc/h boxes shows that the former simulations are converged with respect to resolution effects to about 1% up to scales $k \lesssim 0.6 \text{ h/Mpc}$, and to better than 5% up to scales of $k \lesssim 1 \text{ h/Mpc}$.

respect to emulated spectra obtained from the latest revision of the Cosmic Emulator [52]. While we have a $\sim 5\%$ disagreement with the HALOFIT model, the agreement with the emulated spectra is excellent, and we therefore suspect that HALOFIT tends to overpredict the total matter power for our chosen cosmology. By comparing the simulations for different resolutions, i.e. the 2 Gpc/h and the 0.9 Gpc/h box, we can convince ourselves that we have a $\sim 1\%$ numerical convergence of the absolute matter power in the 2 Gpc/h simulations up to $k \simeq 0.6 \text{ h/Mpc}$, and the resolution effects reach $\sim 5\%$ only for $k \gtrsim 1 \text{ h/Mpc}$. This agrees well with our expectation that resolution effects on the power spectrum scale as k^2/k_{Ny}^2 at leading order, where $k_{\text{Ny}} = \pi / (0.5 \text{ Mpc/h})$ is the Nyquist wavenumber corresponding to the resolution of the simulation. It would therefore seem that e.g. the $\sim 2\%$ feature at $k \simeq 0.5 \text{ h/Mpc}$ in the ratio with respect to the emulated spectrum is actually robust. However, this is well within the error budget of 4% claimed for the Cosmic Emulator.

It is worth noting that the emulated spectrum seems to have some slight shape issues in the case of massive neutrinos. In particular, it shows a noticeable excess of power ($P_{\text{N-body}}/P_{\text{model}} < 1$) around $k \simeq 0.04 \text{ h/Mpc}$ where HALOFIT always agrees with our numerical results from the large-volume simulations. This $\sim 2\%$ feature is absent for the case

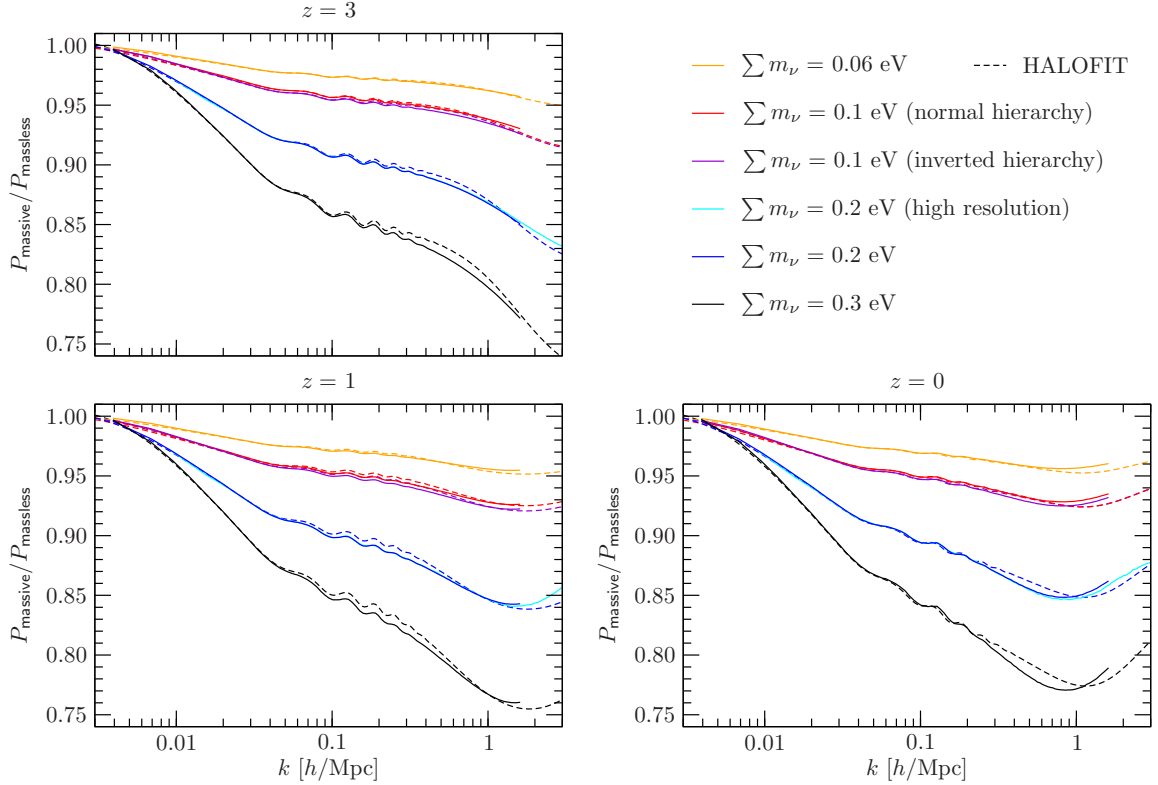


Figure 7. At three different redshifts we show the ratio of the numerical total matter power obtained for various neutrino masses relative to the massless case. The numerical data was taken from the runs with $L_{\text{box}} = 2 \text{ Gpc}/h$, except for the light blue curve showing the result for the runs with $L_{\text{box}} = 0.9 \text{ Gpc}/h$ that have twice the resolution. The latter indicates that the relative spectra are converged to better than 1% for all $k \lesssim 1 \text{ h}/\text{Mpc}$. Dashed lines show the corresponding predictions from the HALOFIT model.

of massless neutrinos. After discussing with one of the authors of [52] we think this is due to the way the emulator is matched to linear theory on large scales. As a consequence of this issue the Cosmic Emulator, despite clearly outperforming HALOFIT in absolute terms, is not well suited when taking ratios of emulated spectra in order to study the relative impact of neutrino masses. The HALOFIT model may be 5% off in absolute terms, but the shape of this error seems to be less dependent on the neutrino mass.

The relative change in the total matter power due to the neutrino masses is shown in Figure 7 for redshifts $z = 3, 1, \text{ and } 0$. Our resolution study indicates that these results are converged to better than 1% for all scales $k \lesssim 1 \text{ h}/\text{Mpc}$. This can be understood from the expectation that the leading-order term in the resolution effect will almost cancel when taking the ratio. To see this, let us schematically write

$$P_{\text{N-body}}(k) \simeq P_{\text{continuum}}(k) \left(1 + c \frac{k^2}{k_{\text{Ny}}^2} + \dots \right) \quad (5.1)$$

where c is a coefficient of order unity, and the ellipsis stands for higher-order corrections. If we now take the ratio of two numerical power spectra one sees that the correction term $\propto k^2/k_{\text{Ny}}^2$ appears with a coefficient $(c_1 - c_2)$, where c_1, c_2 are the respective coefficients for the two

spectra in question. It appears reasonable to expect that these do not strongly depend on cosmology and hence $|c_1 - c_2| \ll |c_1|, |c_2|$. In other words, resolution effects are partially removed when taking ratios of spectra.

Since we keep the total matter density fixed as we vary the neutrino mass, the neutrinos generally lead to a suppression of the power on scales smaller than their free-streaming length. The suppression is roughly proportional to the sum of the masses. Intuitively this makes sense since it is the fractional contribution of neutrinos to the total matter which is relevant here. Due to free streaming the neutrinos constitute a matter component that is much more smoothly distributed than CDM (cf. Figure 1). Furthermore, since the gravitational potential is sourced by total matter, the onset of nonlinear evolution is delayed. This explains why the nonlinear scales are more sensitive to the neutrino mass. At the other end of the spectrum, at extremely large scales that are outside of the free-streaming scale, neutrinos effectively behave as CDM and hence a change of their mass has nearly no effect.

Our results show that the relative suppression of matter power is reasonably well modelled by the HALOFIT recipe. The largest disagreement is seen on mildly nonlinear scales, $0.1 h/\text{Mpc} \lesssim k \lesssim 1 h/\text{Mpc}$, and can reach $\sim 1\%$. On these scales HALOFIT generally underestimates the amount of suppression. Our simulations also indicate that the maximal power suppression is reached at slightly larger scales than predicted by HALOFIT. Furthermore, we demonstrate that our simulations can distinguish the mass hierarchy at $\sum m_\nu = 0.1 \text{ eV}$ which is not fully incorporated in the HALOFIT recipe. The hierarchy has an effect of the order of half a per cent on nonlinear scales, in agreement to what has been found in [53].

6 Power spectra of relativistic potentials

In our relativistic N-body code we also calculate the induced vector and tensor perturbations of the metric as well as the gravitational slip. As we have seen in the previous section, the free-streaming of massive neutrinos gives rise to a suppression of small-scale power that generally also leads to a suppression of these relativistic effects, as they are mainly sourced by the nonlinearities in the matter distribution which are strongest on small scales. On the other hand, neutrinos themselves initially have very high velocities which, as we will discuss below, gives rise to gravitational slip at large scales.

6.1 Scalar potentials

In Newtonian gravity the two Bardeen potentials ϕ and ψ are equal and they are equal to the Newtonian potential. In general relativity they are different and we denote their difference by $\chi = \phi - \psi$. Within linear perturbation theory χ is sourced by the scalar anisotropic stress of relativistic species, i.e. photons and relativistic neutrinos. However, this contribution is strongly damped by free-streaming inside the sound horizon, and after the end of radiation domination the second-order anisotropic stress of CDM starts to dominate on most scales. Only on very large scales the first-order relativistic contribution remains dominant for a long time. In Figure 8 we show the various contributions at redshift $z = 15$ computed in first and second order perturbation theory, together with our nonperturbative numerical result (shot noise is removed using the technique discussed in Section 5). It is worth noting that our neutrino N-body ensemble gives rise to the expected linear effect at very large scales. We plot the dimensionless power spectra defined by

$$\Delta(k) = 4\pi k^3 P(k). \quad (6.1)$$

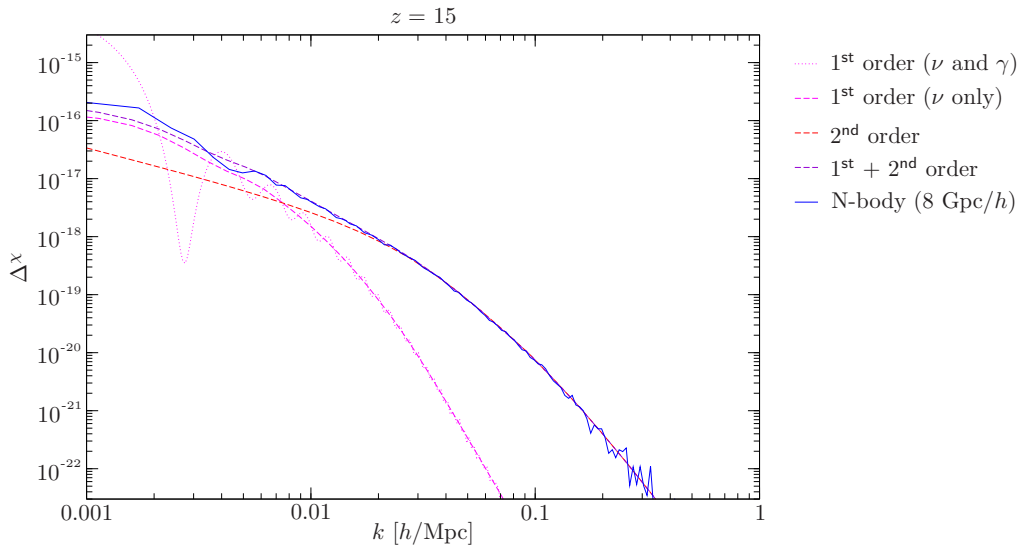


Figure 8. At redshift $z = 15$ we show the most important contributions to the power spectrum of χ for a cosmology with $\sum m_\nu = 0.2$ eV. The magenta dotted line is the total first-order contribution from photons and neutrinos (other species do not have a first-order contribution) as computed by *CLASS*, which is of interest as we neglect the photon perturbations in our simulations. The magenta dashed line is the first-order contribution from neutrinos only as computed by *CLASS*. At second order, also CDM, baryons and geometry (in the guise of a weak-field term $\propto \phi_{,i}\phi_{,j}$) contribute, plotted as red dashed line. The corresponding expression is given in Appendix B. The violet dashed line is the total of first and second order, neglecting photons. Our simulation result, shown in blue, is in excellent agreement with this perturbative prediction. Note in particular that the neutrino N-body ensemble provides the required amount of anisotropic stress at large scales.

As the neutrinos cool down, their anisotropic stress decays and eventually becomes very subdominant and their main effect then is the reduction of small scale power and therefore of non-linearities which are the main source of χ at late times. At late times, massive neutrinos hence induce a significant suppression to the χ -spectrum, see Figure 9. Especially on small scales there is an important suppression of the numerical power-spectrum due to non-linearities compared to the second order result (shown as dashed lines).

In Figure 10 we compare the ratios $\Delta_{\text{massive}}^\chi(k)/\Delta_{\text{massless}}^\chi(k)$ at $z = 0$. The difference is largest, about 50%, for the highest mass, $\sum m_\nu = 0.3$ eV, and smallest, about 10%, for the smallest mass, $\sum m_\nu = 0.06$ eV. Note the slight difference between the normal and inverted hierarchy for $\sum m_\nu = 0.1$ eV. We have also found that the relative difference of the spectra increases with time and that its maximum moves slowly to larger scales from $k_{\text{max}} \sim 4$ h/Mpc at redshift $z = 3$ to $k_{\text{max}} \sim 0.7$ h/Mpc at redshift $z = 0$. The same behavior is also visible in other spectra. Once a scale has become very non-linear, the effects of neutrino damping become less important.

In Figure 11 we show the difference between the Weyl potential, $(\phi + \psi)/2$ and the Newtonian potential ψ for massive and massless neutrinos. As becomes clear from the lower panel, the change in this difference is quite relevant, about 50%. On the other hand, it agrees rather well with the result expected from linear perturbation theory computed with *CLASS* (green line). On small scales, when non-linearities are generated, this difference which is

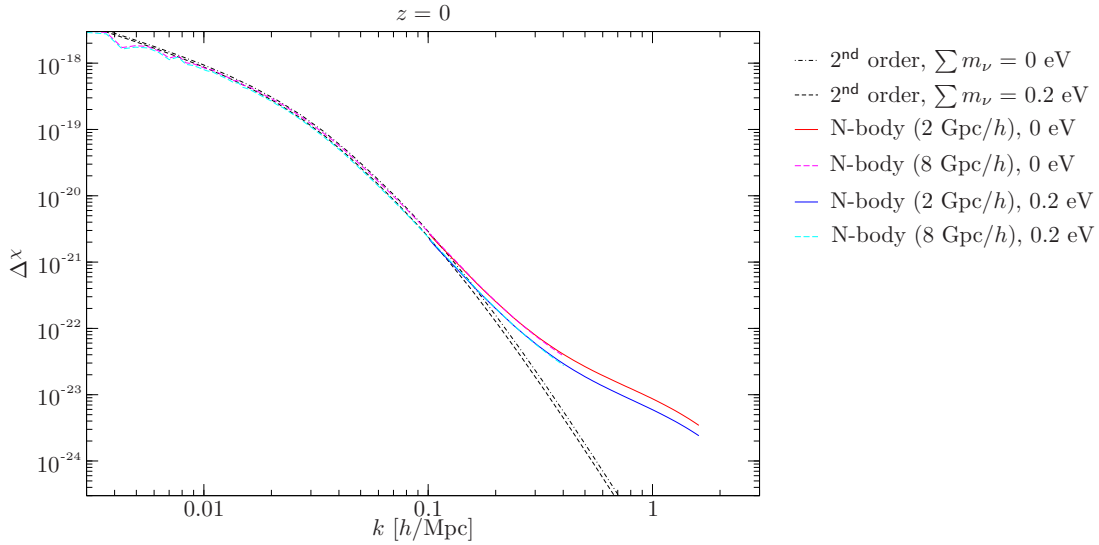


Figure 9. We show the dimensionless power spectra of χ at redshift $z = 0$ for a cosmology with $\sum m_\nu = 0.2$ eV compared to the case of massless neutrinos. As expected from a second-order calculation (black dashed and dash-dotted lines) the power is lower in the massive case as a result of the damping of matter perturbations. The first-order anisotropic stress of the neutrino component has decayed and can now be neglected against the second-order contribution from CDM even at large sub-horizon scales.

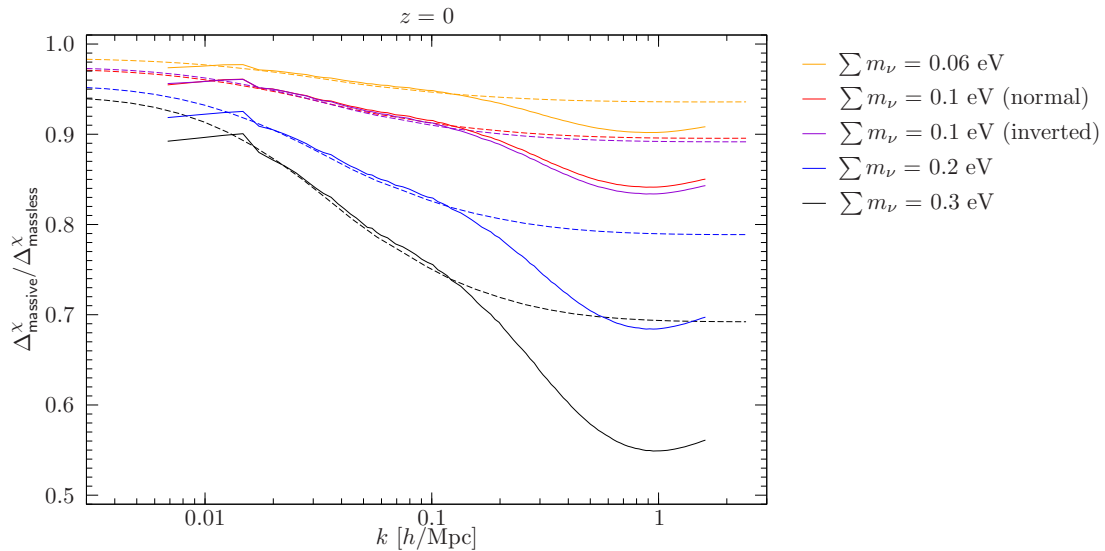


Figure 10. We show the ratios of the χ -spectra for different neutrino masses with respect to the massless case at redshift $z = 0$. The solid curves are obtained from our relativistic N-body simulations with a 2 Gpc/h comoving box. The dashed lines show the corresponding predictions from a second-order calculation. The onset of non-linear clustering at $k \gtrsim 0.1 h/\text{Mpc}$ is clearly visible. The power suppression in χ is stronger than in the total matter power spectra, shown in Figure 7.

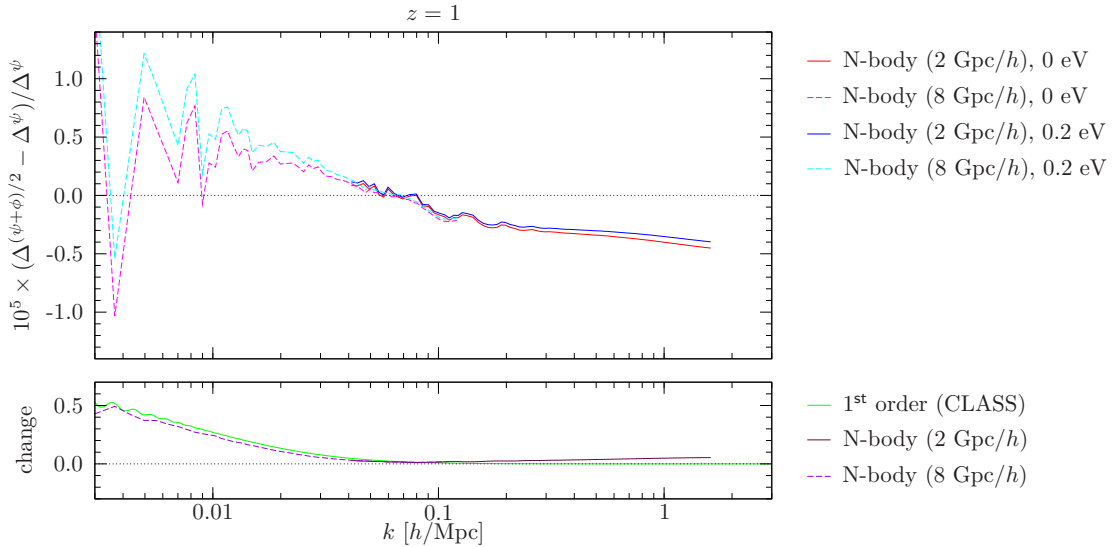


Figure 11. We show the relative difference (multiplied by 10^5) between the power spectra of the Weyl potential $(\psi + \phi)/2$ and the first Bardeen potential ψ for massless neutrinos and for the case $\sum m_\nu = 0.2$ eV at redshift $z = 1$ (upper panel). The lower panel shows the change of this quantity between the two cases (in the same units). At large scales, most of the change is due to the first-order anisotropic stress in the neutrino component.

purely due to neutrino anisotropic stresses is less important, and of the order of 5%. Photons respond to the Weyl potential while massive particles respond to ψ ; to see this compare the geodesic equation (2.9) in the limits $q^2 \gg m^2 a^2$ and $q^2 \ll m^2 a^2$. Therefore this difference is in principle testable. This effect is much larger for modified gravity theories but it is important to keep in mind that it is also present in the standard model, albeit with a very small amplitude of about 10^{-5} (see also [54]).

6.2 Vector potential

As we have already found previously [21, 23], the vector perturbations of the metric are the largest relativistic signature. In amplitude they reach about 1% of the scalar perturbations and might therefore in principle be detectable (even though so far a good idea to specifically detect these vector modes is still lacking).

In Figure 12 we show the spectra of vector perturbations at redshift $z = 0$ for simulations with $\sum m_\nu = 0.2$ eV and with massless neutrinos. The results from a second order calculation are also shown. In Figure 13 we show the ratio $\Delta_{\text{massive}}^B(k)/\Delta_{\text{massless}}^B(k)$ at $z = 0$ for neutrino masses from $\sum m_\nu = 0.3$ eV down to $\sum m_\nu = 0.06$ eV. Again the difference is largest for the largest neutrino mass. For $\sum m_\nu = 0.3$ eV the B -power spectrum is reduced by about 30% at the scale $k \simeq 0.7 h/\text{Mpc}$. But also for the smallest neutrino mass we have considered, $\sum m_\nu = 0.06$ eV, the reduction still reaches about 5%.

We have found that the difference in the spectra increases with decreasing redshift on large to intermediate scales. On small scales, $k \lesssim 1 h/\text{Mpc}$ the trend is reversed at late time, like for the Newtonian gravitational potential. On these small scales, at late times non-linearities become sufficiently strong so that clustering with neutrinos slowly catches up with the pure CDM case.

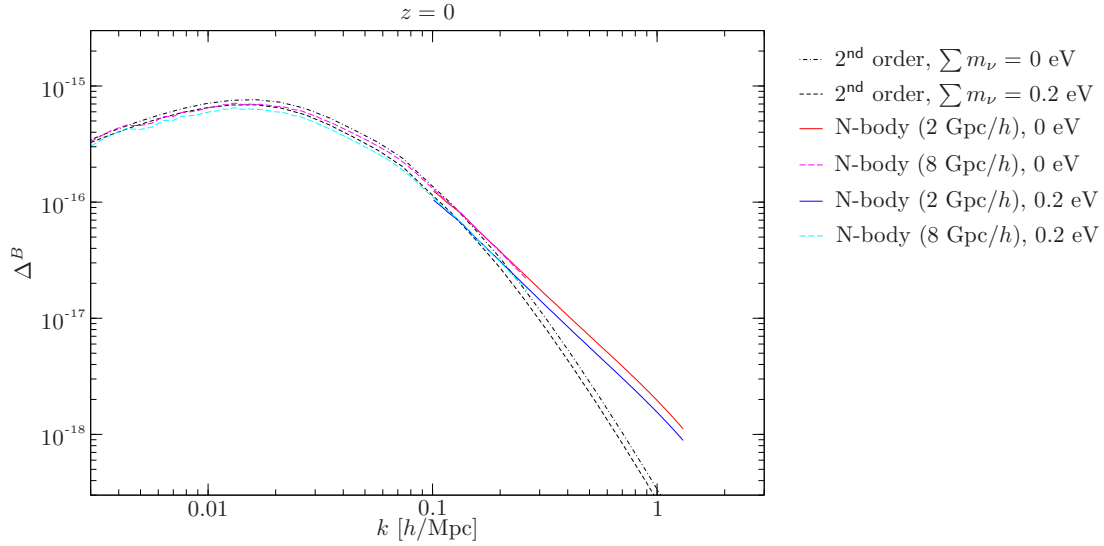


Figure 12. The vector spectra at redshift $z = 0$ for a massless neutrino cosmology and one with $\sum m_\nu = 0.2$ eV. As in Figure 9 we also show the second-order calculation (black dashed and dash-dotted lines, see Appendix B) indicating the general trend: the damping of matter perturbations reduces the amplitude of the relativistic potentials.

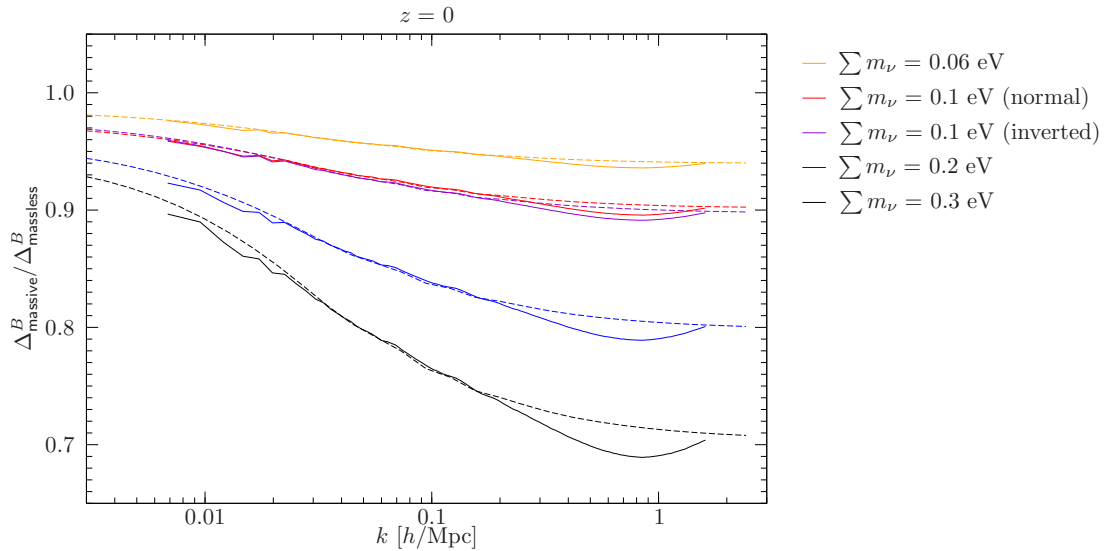


Figure 13. The ratios of the vector spectra for various neutrino masses with respect to the massless case at redshift $z = 0$. The solid curves are obtained from our relativistic N-body simulations with a 2 Gpc/h comoving box. The dashed lines show the corresponding predictions from a second-order calculation.

6.3 Tensor perturbations

In Figure 14 we show the tensor power spectrum at redshift $z = 0$ for simulations with $\sum m_\nu = 0.2$ eV and for massless neutrinos. The second order perturbative result is also indicated as dashed line. In Figure 15 we show the ratio $\Delta_{\text{massive}}^h(k)/\Delta_{\text{massless}}^h(k)$ for all masses investigated. Again, the difference is largest for the largest neutrino mass, $\sum m_\nu = 0.3$ eV, where it amounts to about 40% on small scales, $k \gtrsim 0.8$ h/Mpc. But also for the smallest neutrino mass we have looked at, $\sum m_\nu = 0.06$ eV, the difference is still nearly 10%. The difference between the normal and the inverted hierarchy, however, does not rise above about 1% like also for the other spectra.

Finally, we want to stress that these tensor modes are not gravitational waves in the usual sense of the term. They are not freely propagating but they are actually the adiabatic response of spacetime to the presence of a slowly varying source, the tensor anisotropic stress of matter. Their time dependence is not wave-like so that one cannot detect these tensor modes in a LIGO-like interferometric experiment.

We have seen in this section that the differences between the relativistic spectra without and with neutrino masses are quite important, up to about 40% for the tensor spectra, 30% for the vector spectra, 50% for the χ -spectra and, correspondingly, for the difference between the Weyl potential and the Newtonian potential. Even for the minimal neutrino masses allowed by the oscillation data, the impact is substantial (up to 5%-10%) and persists over a wide range of scales. However, these spectra are all significantly suppressed with respect to the dominant Newtonian gravitational potential spectrum by at least four orders of magnitude and none of them has been measured so far at cosmological scales. The most promising is the vector spectrum which is up to 22% smaller in the presence of massive neutrinos with a total mass of $\sum m_\nu = 0.2$ eV. The amplitude of the vector spectrum is about 1% of the Newtonian potential and the difference in the amplitude is about half the difference of the spectrum which would lead to a 10% effect in the B-mode amplitude or a 0.1% effect on the total gravitational field. This is probably not measurable without a new, groundbreaking idea of how to extract a vector signal.

The relative difference between the Weyl potential and the Newtonian potential is about 10^{-5} on large scales. The tensor power spectrum is two orders of magnitude smaller than the vector signal and the χ -spectrum is about three orders of magnitude smaller. Their detection is correspondingly even more difficult.

7 Halo mass function

Owing to the fact that *gevolution* works at fixed spatial resolution it is not very well suited for studying CDM halos in great detail. However, the resolution achieved in our production runs is sufficient to obtain robust results for some global properties of massive halos, e.g. their virial masses and radii. In Figure 16 we show the halo mass functions obtained at redshift $z = 0$ for the case of massless neutrinos and the one with $\sum m_\nu = 0.2$ eV. In both cases we use snapshots from simulations at two different resolutions in order to check for resolution effects. The lack of adaptive force resolution attenuates the formation of small structures whereas more massive objects will be less affected. Moreover, the virial mass is defined through a spherical overdensity threshold and will have large errors for objects whose virial radius is not well resolved. As expected, the halo mass function is therefore most robust at high masses. For those we obtain results that are converged to better than 10% over a range of more than one order of magnitude in mass.

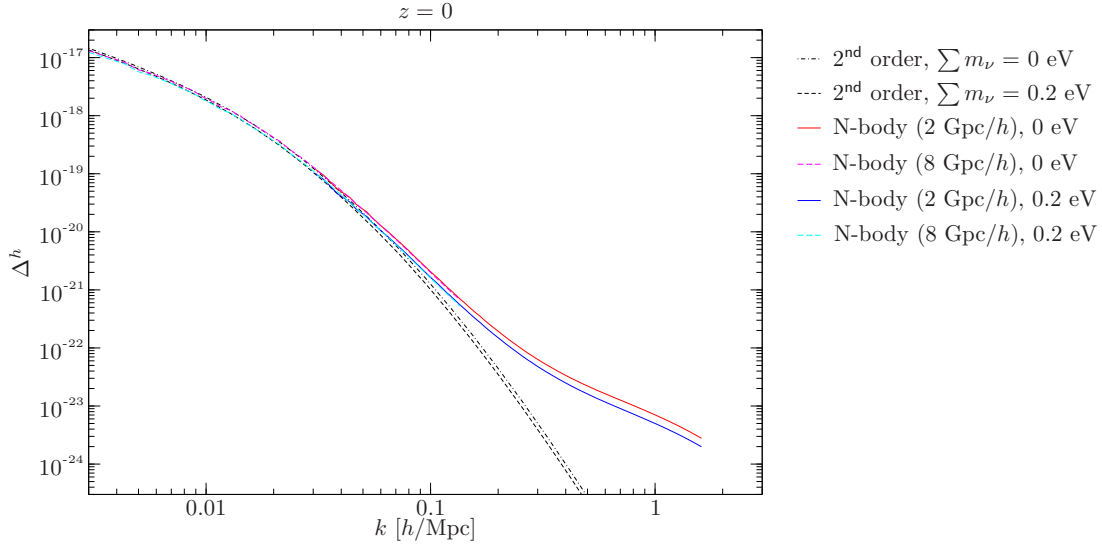


Figure 14. The tensor spectra at redshift $z = 0$ for a massless neutrino cosmology and for one with $\sum m_\nu = 0.2$ eV. The predictions from the second-order calculation (see Appendix B) are also shown.

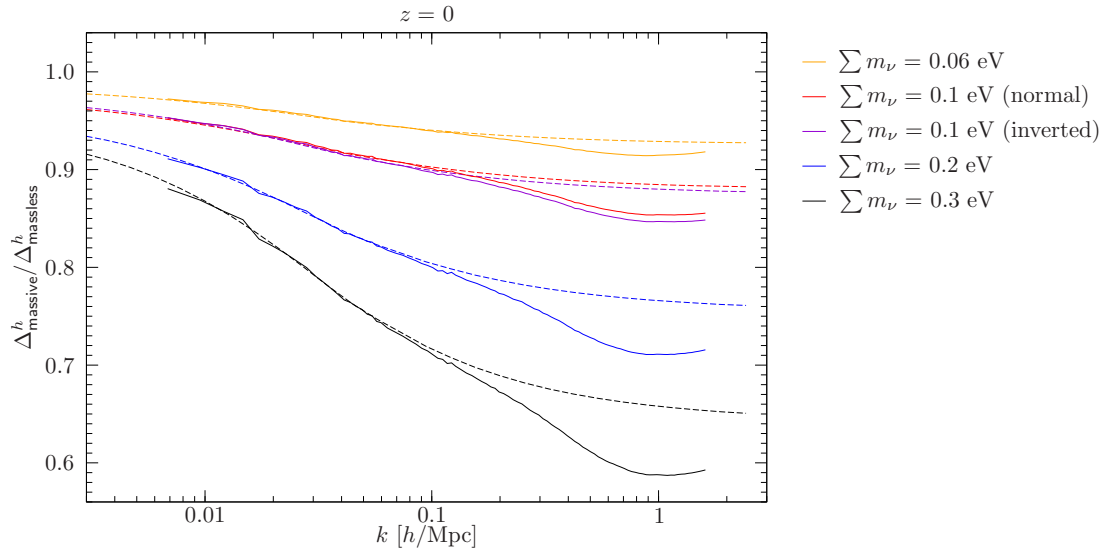


Figure 15. We show the ratios of the spectra of the spin-2 metric perturbation for various neutrino masses with respect to the massless case at redshift $z = 0$. The solid curves are obtained from our relativistic N-body simulations with a 2 Gpc/ h comoving box. The dashed lines show the corresponding predictions from a second-order calculation.

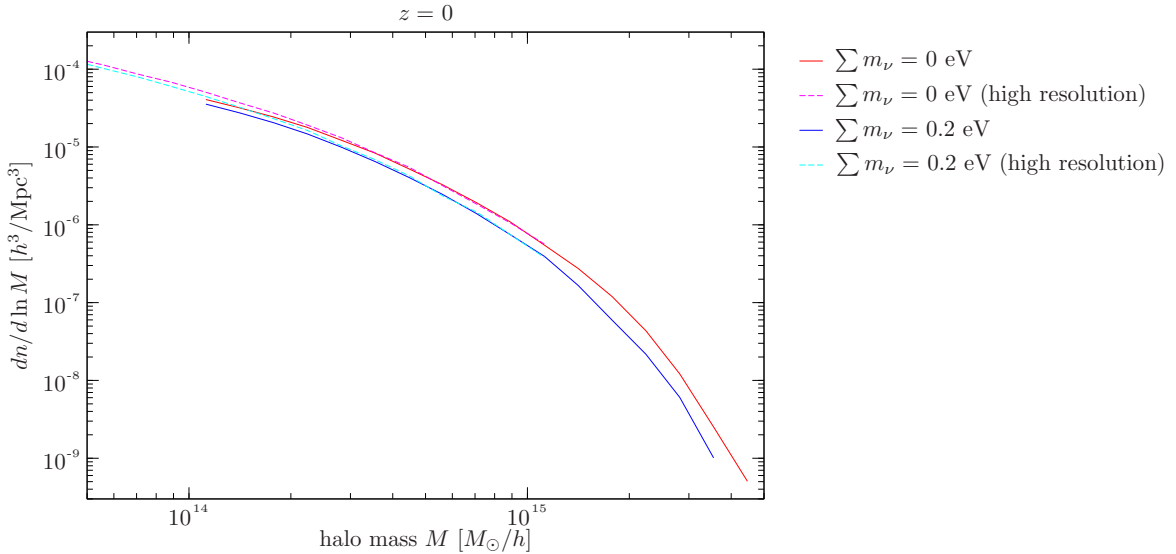


Figure 16. We show the halo mass function measured at redshift $z = 0$ for the case of massless neutrinos and the one with $\sum m_\nu = 0.2$ eV. The halo catalogs were obtained from snapshots of the simulations with 2 Gpc/ h (solid lines) and 0.9 Gpc/ h (dashed lines) boxes. The latter have a higher resolution and hence we can conclude that the numerical results are contaminated by resolution effects of less than $\sim 10\%$ for halo masses $M \gtrsim 3 \times 10^{14} M_\odot/h$.

In line with the general trends discussed so far the mass fraction of neutrinos in the total matter leads to a suppression of the growth of structure as neutrinos free-stream out of the potential wells. The number counts of the most massive objects are therefore affected as shown in Figure 17. Within the range of neutrino masses explored in our study we find that the number count of very massive clusters above $10^{15} M_\odot/h$ varies by up to a factor of two. These results are in good qualitative agreement with the ones found previously in [45].

8 Conclusion

In this paper we present results from a suite of cosmological N-body simulations with massive neutrinos, carried out with our relativistic particle-mesh code *gevolution*. This novel approach allows us for the first time to perform such simulations fully self-consistently within the framework of general relativity, extending in particular to aspects of gauge choice and setting of initial conditions. The N-body phase space is evolved correctly using a weak-field description that is valid for arbitrary momenta, and hence we are able to take into account the relativistic nature of neutrino particles. Furthermore, the approach also allows us to extract the additional five gravitational degrees of freedom beyond the Newtonian potential.

We explore six different scenarios for the neutrino mass eigenstates, including as reference the massless case often assumed in standard cosmology. For the runs with massive neutrinos we consider $\sum m_\nu = 0.06$ eV (a scenario close to the lowest mass compatible with neutrino flavour oscillations as seen by particle physics experiments), $\sum m_\nu = 0.1$ eV (two cases, representing normal and inverted mass hierarchy, respectively), $\sum m_\nu = 0.2$ eV, and $\sum m_\nu = 0.3$ eV (close to the highest mass compatible with cosmological constraints). At the level of the

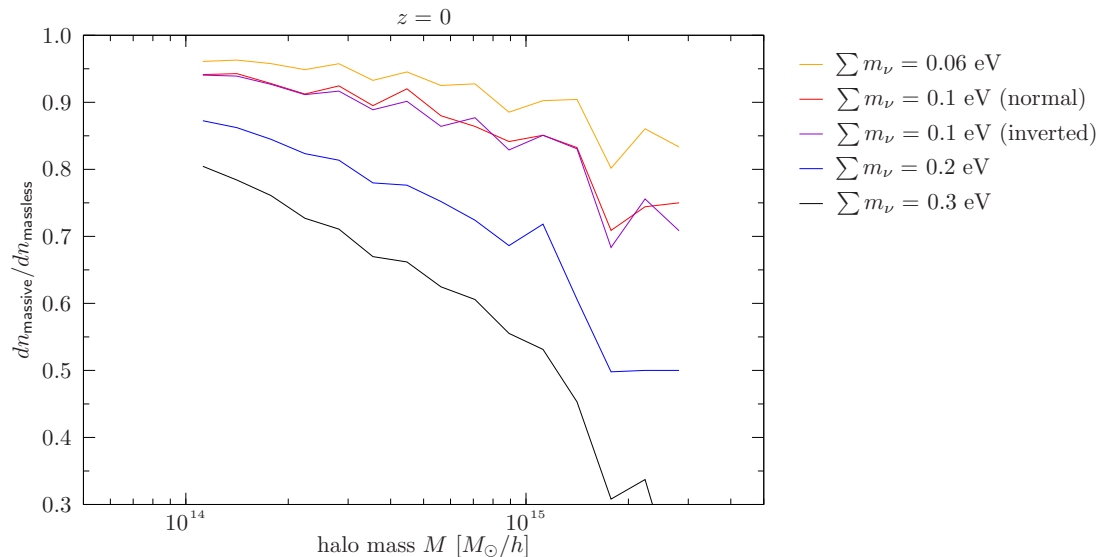


Figure 17. In order to quantify the relative impact of the neutrino mass we show the ratio of the halo mass functions at redshift $z = 0$ for different neutrino masses with respect to the massless case. The change is most dramatic for the highest halo masses.

power spectra of total matter and neutrinos our relativistic results at low redshift generally show good agreement with those obtained with Newtonian methods, at least when we consider scales deep inside the cosmological horizon. More specifically, the nonlinear recipes provided by HALOFIT and the latest revision of the Cosmic Emulator, which are both calibrated to Newtonian simulations, are confirmed to perform to specifications for the cases explored in this paper. While the Cosmic Emulator achieves a better absolute accuracy on the total matter power spectrum, we find that HALOFIT is still better suited when studying the relative suppression of power in the presence of massive neutrinos. This is a consequence of the way the error depends on cosmology in the two recipes.

At fixed total matter density, a larger sum of neutrino masses implies a stronger suppression of power at small scales, as most of the neutrino particles have sufficient thermal energy to stream out of potential wells. Nonlinearities tend to amplify the effect initially, roughly until most of the structure has virialized. For a minimal mass scenario with $\sum m_\nu = 0.06$ eV we find a $\sim 5\%$ suppression of total matter power compared to the case of massless neutrinos around $k \simeq 1$ h/Mpc where the suppression is strongest. The size of the effect increases with neutrino mass, reaching almost 25% for $\sum m_\nu = 0.3$ eV. We find that HALOFIT provides a reasonable model for the relative suppression of power, but tends to underestimate the amount of suppression at intermediate scales 0.1 $h/\text{Mpc} \lesssim k \lesssim 1$ h/Mpc to the effect of changing the result by up to $\sim 1\%$.

The general trend of small scale power suppression also carries forward to the power spectra of the relativistic metric perturbations, i.e. the gravitational slip, the frame-dragging potential, and the tensor perturbation. On large scales the behaviour can be understood from a second-order calculation. There the sources are quadratic in the matter perturbations and therefore the suppression effect is seen to be roughly twice as strong as in the matter power spectrum itself. In addition, neutrinos produce some anisotropic stress already at linear order,

dominating the gravitational slip at high redshift and very large scales. We show that the stress-energy tensor of our neutrino N-body ensemble fully includes this effect. However, the overall amplitude of the relativistic perturbations remains very small, so that it will be very difficult to use them for observational constraints.

We finally also study the halo mass function and are able to confirm that it shows a strong dependence on the neutrino mass at very high halo masses $\gtrsim 10^{15} M_{\odot}/h$. This can provide a means to get additional constraints on the neutrino mass if it is possible to obtain reliable number counts for such rare, extremely massive objects. The neutrino mass hierarchy, on the other hand, seems to have little impact on the halo mass function.

In the future it would be interesting to use our numerical approach to study the regime around the free-streaming scale of neutrinos in more detail. Newtonian simulations are expected to have some subtle issues there because their neutrino propagation violates causality. Even if this is rectified (e.g. according to our recipe given in Section 3) there remain the relativistic effects due to gauge choice and the presence of radiation perturbations that are difficult to deal with in a Newtonian scheme. Future observations at high redshifts, e.g. 21cm surveys [55] at z up to 10 will potentially be sensitive to such issues. The latest version 1.1 of our relativistic code *gevolution*, available at <https://github.com/gevolution-code/gevolution-1.1.git>, provides a self-consistent treatment of all these aspects.

Acknowledgments

We thank K. Heitmann, J. Lesgourgues, V. Poulin, T. Tram and M. Viel for valuable input, and D. Daverio for continued technical support related to the LATfield2 library [56] and its interface with *gevolution*. This work was supported by a grant from the Swiss National Supercomputing Centre (CSCS) under project ID s710. RD and MK also received support from the Swiss National Science Foundation.

This is an author-created, un-copyedited version of an article published in the Journal of Cosmology and Astroparticle Physics (JCAP). IOP Publishing Ltd is not responsible for any errors or omissions in this version of the manuscript or any version derived from it. The Version of Record is available online at <https://doi.org/10.1088/1475-7516/2017/11/004>.

A Leapfrog integrator for relativistic particles

Symplectic integrators [57] play an important role in the context of N-body simulations. They are defined by the property to preserve the form $d\mathbf{x} \wedge d\mathbf{q}$ exactly, as demanded by Hamiltonian time evolution (in our notation the canonical coordinate is x^i while q_i is the canonical momentum). In our relativistic weak-field setting, the one-particle Hamiltonian giving rise to the Hamiltonian equations of motion (2.9) and (2.10) reads

$$H(x^i, q_i, \tau) = \sqrt{q^2 + m^2 a^2(\tau)} [1 - \chi(x^i, \tau)] + \frac{2q^2 + m^2 a^2(\tau)}{\sqrt{q^2 + m^2 a^2(\tau)}} \phi(x^i, \tau) + q^j B_j(x^i, \tau) - \frac{1}{2} \frac{q^j q^k h_{jk}(x^i, \tau)}{\sqrt{q^2 + m^2 a^2(\tau)}}. \quad (\text{A.1})$$

As explained in Section 2, the last term is expected to be extremely small and we therefore neglect it from now on, even though it can easily be included. The solution to the equations

of motion are computed numerically at discrete time steps. To illustrate this, let us first consider the limit of non-relativistic motion, $q^2 \ll m^2 a^2$, assuming also the post-Newtonian ordering of weak fields $|\phi| \ll 1$, $|\chi| \ll |\phi|$, $\sqrt{B^2} \ll |\phi|$. In this approximation the Hamiltonian becomes

$$H(x^i, q_i, \tau) = ma(\tau) [1 + \phi(x^i, \tau)] + \frac{q^2}{2ma(\tau)}. \quad (\text{A.2})$$

In this case, the Hamiltonian equations of motion are the Newtonian ones, eq. (3.2) and (3.3).

We now introduce an integer label \mathbf{n} that enumerates the discrete time steps $\tau_{\mathbf{n}}$, and we use half-integers to denote midpoints between time steps. A kick-drift-kick scheme for the Newtonian equations reads

$$q_i^{\mathbf{n}+\frac{1}{2}} = q_i^{\mathbf{n}} - \frac{d\tau}{2} ma(\tau_{\mathbf{n}}) \phi_{,i}(x_{\mathbf{n}}^i, \tau_{\mathbf{n}}), \quad (\text{A.3a})$$

$$x_{\mathbf{n}+1}^i = x_{\mathbf{n}}^i + \delta^{ij} d\tau \frac{q_j^{\mathbf{n}+\frac{1}{2}}}{ma(\tau_{\mathbf{n}+\frac{1}{2}})}, \quad (\text{A.3b})$$

$$q_i^{\mathbf{n}+1} = q_i^{\mathbf{n}+\frac{1}{2}} - \frac{d\tau}{2} ma(\tau_{\mathbf{n}+1}) \phi_{,i}(x_{\mathbf{n}+1}^i, \tau_{\mathbf{n}+1}), \quad (\text{A.3c})$$

where we introduced the shorthands $q_i^{\mathbf{n}} \doteq q_i(\tau_{\mathbf{n}})$ and $x_{\mathbf{n}}^i \doteq x^i(\tau_{\mathbf{n}})$. As one can show by direct computation, this update sequence is symplectic. In practice one can avoid the explicit computation of q_i at integer time steps by combining eq. (A.3a) with eq. (A.3c) from the previous time step. The resulting abridged sequence is what we call the leapfrog scheme. We may still call this scheme symplectic even though this property is somewhat implicit.

Let us now consider the relativistic system of equations with q^2 arbitrary. In *gevolution* we use a straightforward generalization of the above leapfrog scheme, which reads

$$q_i^{\mathbf{n}+\frac{1}{2}} = q_i^{\mathbf{n}} - \frac{d\tau}{2} \left[\frac{2q_{\mathbf{n}-\frac{1}{2}}^2 + m^2 a^2(\tau_{\mathbf{n}})}{\sqrt{q_{\mathbf{n}-\frac{1}{2}}^2 + m^2 a^2(\tau_{\mathbf{n}})}} \phi_{,i}(x_{\mathbf{n}}^i, \tau_{\mathbf{n}}) - \sqrt{q_{\mathbf{n}-\frac{1}{2}}^2 + m^2 a^2(\tau_{\mathbf{n}})} \chi_{,i}(x_{\mathbf{n}}^i, \tau_{\mathbf{n}}) - \delta^{jk} q_j^{\mathbf{n}-\frac{1}{2}} B_{k,i}(x_{\mathbf{n}}^i, \tau_{\mathbf{n}}) \right], \quad (\text{A.4a})$$

$$x_{\mathbf{n}+1}^i = x_{\mathbf{n}}^i + \delta^{ij} d\tau \frac{q_j^{\mathbf{n}+\frac{1}{2}}}{\sqrt{q_{\mathbf{n}+\frac{1}{2}}^2 + m^2 a^2(\tau_{\mathbf{n}+\frac{1}{2}})}} \left[1 + \frac{2q_{\mathbf{n}+\frac{1}{2}}^2 + 3m^2 a^2(\tau_{\mathbf{n}+\frac{1}{2}})}{q_{\mathbf{n}+\frac{1}{2}}^2 + m^2 a^2(\tau_{\mathbf{n}+\frac{1}{2}})} \phi(x_{\mathbf{n}}^i, \tau_{\mathbf{n}}) - \chi(x_{\mathbf{n}}^i, \tau_{\mathbf{n}}) \right] + \delta^{ij} d\tau B_j(x_{\mathbf{n}}^i, \tau_{\mathbf{n}}), \quad (\text{A.4b})$$

$$q_i^{\mathbf{n}+1} = q_i^{\mathbf{n}+\frac{1}{2}} - \frac{d\tau}{2} \left[\frac{2q_{\mathbf{n}+\frac{1}{2}}^2 + m^2 a^2(\tau_{\mathbf{n}+1})}{\sqrt{q_{\mathbf{n}+\frac{1}{2}}^2 + m^2 a^2(\tau_{\mathbf{n}+1})}} \phi_{,i}(x_{\mathbf{n}+1}^i, \tau_{\mathbf{n}+1}) - \sqrt{q_{\mathbf{n}+\frac{1}{2}}^2 + m^2 a^2(\tau_{\mathbf{n}+1})} \chi_{,i}(x_{\mathbf{n}+1}^i, \tau_{\mathbf{n}+1}) - \delta^{jk} q_j^{\mathbf{n}+\frac{1}{2}} B_{k,i}(x_{\mathbf{n}+1}^i, \tau_{\mathbf{n}+1}) \right]. \quad (\text{A.4c})$$

Note that the first and last step are constructed in a way that we can again avoid an explicit computation of q_i at the integer time step. This is possible because q_i is time-independent at

the background level and can therefore be evaluated at any time for the purpose of constructing the prefactors of weak-field terms. We remind the reader that we only go to first order in the gravitational fields for the purpose of solving the equations of motion of the particles.

The scheme defined by eqs. (A.4a)–(A.4c) is not exactly symplectic, yet symplecticity is recovered in the limit of small velocities and post-Newtonian ordering of the weak fields. This is sufficient for the purpose of this work. However, with a simple adjustment of the drift step it is possible to make the scheme symplectic at leading weak-field order even for relativistic velocities. All we need to do is replace eq. (A.4b) by its second-order version,

$$\begin{aligned}
x_{\mathbf{n}+1}^i &= x_{\mathbf{n}}^i + \delta^{ij} \frac{d\tau}{2} \frac{q_j^{\mathbf{n}+\frac{1}{2}}}{\sqrt{q_{\mathbf{n}+\frac{1}{2}}^2 + m^2 a^2(\tau_{\mathbf{n}})}} \left[1 + \frac{2q_{\mathbf{n}+\frac{1}{2}}^2 + 3m^2 a^2(\tau_{\mathbf{n}})}{q_{\mathbf{n}+\frac{1}{2}}^2 + m^2 a^2(\tau_{\mathbf{n}})} \phi(x_{\mathbf{n}}^i, \tau_{\mathbf{n}}) - \chi(x_{\mathbf{n}}^i, \tau_{\mathbf{n}}) \right] \\
&+ \delta^{ij} \frac{d\tau}{2} \frac{q_j^{\mathbf{n}+\frac{1}{2}}}{\sqrt{q_{\mathbf{n}+\frac{1}{2}}^2 + m^2 a^2(\tau_{\mathbf{n}+1})}} \left[1 + \frac{2q_{\mathbf{n}+\frac{1}{2}}^2 + 3m^2 a^2(\tau_{\mathbf{n}+1})}{q_{\mathbf{n}+\frac{1}{2}}^2 + m^2 a^2(\tau_{\mathbf{n}+1})} \phi(\tilde{x}_{\mathbf{n}+1}^i, \tau_{\mathbf{n}+1}) - \chi(\tilde{x}_{\mathbf{n}+1}^i, \tau_{\mathbf{n}+1}) \right] \\
&+ \delta^{ij} \frac{d\tau}{2} B_j(x_{\mathbf{n}}^i, \tau_{\mathbf{n}}) + \delta^{ij} \frac{d\tau}{2} B_j(\tilde{x}_{\mathbf{n}+1}^i, \tau_{\mathbf{n}+1}), \quad (\text{A.5})
\end{aligned}$$

where

$$\tilde{x}_{\mathbf{n}+1}^i \doteq x_{\mathbf{n}}^i + \delta^{ij} \frac{d\tau}{2} \frac{q_j^{\mathbf{n}+\frac{1}{2}}}{\sqrt{q_{\mathbf{n}+\frac{1}{2}}^2 + m^2 a^2(\tau_{\mathbf{n}})}} + \delta^{ij} \frac{d\tau}{2} \frac{q_j^{\mathbf{n}+\frac{1}{2}}}{\sqrt{q_{\mathbf{n}+\frac{1}{2}}^2 + m^2 a^2(\tau_{\mathbf{n}+1})}} \quad (\text{A.6})$$

is the zeroth-order approximation for the new position. A lengthy but straightforward calculation shows that this drift step fully restores symplecticity at leading weak-field order. Unfortunately the position update now depends on the metric at final time $\tau_{\mathbf{n}+1}$ as well, which is usually not available as it will be computed only from the final particle configuration. This issue can be solved using a predictor-corrector method. If the metric perturbations are time-independent to good approximation, one may simply use the values from the previous time step. In any case the number of field interpolation operations will be doubled compared to the simpler drift step (A.4b). For this reason, and since deviations from symplecticity are anyway small and tend to zero for low velocities, we use the simpler integrator defined by eqs. (A.4a)–(A.4c) in our work.

B Second-order contributions to the relativistic potentials

Here we collect the expressions for the convolution integrals that give the second-order contributions to the relativistic metric perturbations $\chi = \phi - \psi$, B_i , and h_{ij} . The principles behind this calculation have been laid out in previous work [54, 58, 59] and where necessary we generalize these to the case of multiple matter species. We also note that the growth rate is no longer independent of scale if massive neutrinos are present, which otherwise allows for some simplifications. Based on the derivation given in the appendix of [24], the second-order contribution to the power spectrum of χ is given by

$$\begin{aligned}
\Delta_{(2)}^\chi(k) &= \frac{1}{2\pi k^5} \int d^3 \mathbf{q} \left[T_q^\phi T_{|\mathbf{k}-\mathbf{q}|}^\phi + 4\pi G a^2 \sum_i \bar{\rho}_i \frac{T_q^{\theta,i}}{q^2} \frac{T_{|\mathbf{k}-\mathbf{q}|}^{\theta,i}}{|\mathbf{k}-\mathbf{q}|^2} \right]^2 \frac{\Delta_{\zeta,\text{in}}(q)}{q^3} \frac{\Delta_{\zeta,\text{in}}(|\mathbf{k}-\mathbf{q}|)}{|\mathbf{k}-\mathbf{q}|^3} \\
&\times \left[3(\mathbf{q}\cdot\mathbf{k})^2 - 2k^2(\mathbf{q}\cdot\mathbf{k}) - k^2 q^2 \right]^2, \quad (\text{B.1})
\end{aligned}$$

where $\Delta^{\zeta,\text{in}}$ is the initial power spectrum of the gauge-invariant curvature perturbation, and T_k^ϕ , $T_k^{\theta,i}$ are the linear transfer functions of ϕ and the divergence of the velocity for the i th matter species, respectively.

The tensor perturbation h_{ij} follows from the spin-2 projection of the same subset of Einstein's equations, and hence one obtains a very similar expression,

$$\Delta_{(2)}^h(k) = \frac{1}{2\pi k^5} \int d^3\mathbf{q} \left[T_q^\phi T_{|\mathbf{k}-\mathbf{q}|}^\phi + 4\pi G a^2 \sum_i \bar{\rho}_i \frac{T_q^{\theta,i}}{q^2} \frac{T_{|\mathbf{k}-\mathbf{q}|}^{\theta,i}}{|\mathbf{k}-\mathbf{q}|^2} \right]^2 \frac{\Delta^{\zeta,\text{in}}(q)}{q^3} \frac{\Delta^{\zeta,\text{in}}(|\mathbf{k}-\mathbf{q}|)}{|\mathbf{k}-\mathbf{q}|^3} \times 8 \left[(\mathbf{q}\cdot\mathbf{k})^2 - k^2 q^2 \right]^2, \quad (\text{B.2})$$

see appendix B of [22] for more details. The only difference is the structure of the term in the second line.

The frame-dragging potential B_i is obtained from the transverse projection of the momentum constraint. At second order the resulting expression reads

$$\Delta_{(2)}^B(k) = \frac{4}{\pi k^3} (4\pi G a^2)^2 \int d^3\mathbf{q} \left[\sum_i \bar{\rho}_i \frac{T_q^{\theta,i}}{q^2} T_{|\mathbf{k}-\mathbf{q}|}^{\delta,i} \right] \left[\sum_j \bar{\rho}_j \left(\frac{T_{|\mathbf{k}-\mathbf{q}|}^{\theta,j}}{|\mathbf{k}-\mathbf{q}|^2} T_q^{\delta,j} - \frac{T_q^{\theta,j}}{q^2} T_{|\mathbf{k}-\mathbf{q}|}^{\delta,j} \right) \right] \times \frac{\Delta^{\zeta,\text{in}}(q)}{q^3} \frac{\Delta^{\zeta,\text{in}}(|\mathbf{k}-\mathbf{q}|)}{|\mathbf{k}-\mathbf{q}|^3} \left[(\mathbf{q}\cdot\mathbf{k})^2 - k^2 q^2 \right], \quad (\text{B.3})$$

where $T_k^{\delta,i}$ are the linear transfer functions for the density perturbations.

References

- [1] **CMS** Collaboration, S. Chatrchyan et al., *Observation of a new boson at a mass of 125 GeV with the CMS experiment at the LHC*, *Phys. Lett.* **B716** (2012) 30–61, [[arXiv:1207.7235](#)].
- [2] **ATLAS** Collaboration, G. Aad et al., *Observation of a new particle in the search for the Standard Model Higgs boson with the ATLAS detector at the LHC*, *Phys. Lett.* **B716** (2012) 1–29, [[arXiv:1207.7214](#)].
- [3] T. Kajita, *Nobel Lecture: Discovery of atmospheric neutrino oscillations*, *Rev. Mod. Phys.* **88** (2016), no. 3 030501.
- [4] A. B. McDonald, *Nobel Lecture: The Sudbury Neutrino Observatory: Observation of flavor change for solar neutrinos*, *Rev. Mod. Phys.* **88** (2016), no. 3 030502.
- [5] **Double Chooz** Collaboration, Y. Abe et al., *Indication of Reactor $\bar{\nu}_e$ Disappearance in the Double Chooz Experiment*, *Phys. Rev. Lett.* **108** (2012) 131801, [[arXiv:1112.6353](#)].
- [6] **LSND** Collaboration, A. Aguilar-Arevalo et al., *Evidence for neutrino oscillations from the observation of anti-neutrino(electron) appearance in a anti-neutrino(muon) beam*, *Phys. Rev.* **D64** (2001) 112007, [[hep-ex/0104049](#)].
- [7] G. Mention, M. Fechner, T. Lasserre, T. A. Mueller, D. Lhuillier, M. Cribier, and A. Letourneau, *The Reactor Antineutrino Anomaly*, *Phys. Rev.* **D83** (2011) 073006, [[arXiv:1101.2755](#)].
- [8] **MiniBooNE** Collaboration, A. A. Aguilar-Arevalo et al., *Improved Search for $\bar{\nu}_\mu \rightarrow \bar{\nu}_e$ Oscillations in the MiniBooNE Experiment*, *Phys. Rev. Lett.* **110** (2013) 161801, [[arXiv:1303.2588](#)].

- [9] G. J. Feldman, J. Hartnell, and T. Kobayashi, *Long-baseline neutrino oscillation experiments*, *Adv. High Energy Phys.* **2013** (2013) 475749, [[arXiv:1210.1778](#)].
- [10] **Particle Data Group** Collaboration, C. Patrignani et al., *Review of Particle Physics*, *Chin. Phys.* **C40** (2016), no. 10 100001.
- [11] J. Lesgourgues and S. Pastor, *Massive neutrinos and cosmology*, *Phys. Rept.* **429** (2006) 307–379, [[astro-ph/0603494](#)].
- [12] **DESI** Collaboration, M. Levi et al., *The DESI Experiment, a whitepaper for Snowmass 2013*, [[arXiv:1308.0847](#)].
- [13] **EUCLID** Collaboration, R. Laureijs et al., *Euclid Definition Study Report*, [[arXiv:1110.3193](#)].
- [14] **Euclid Theory Working Group** Collaboration, L. Amendola et al., *Cosmology and fundamental physics with the Euclid satellite*, *Living Rev. Rel.* **16** (2013) 6, [[arXiv:1206.1225](#)].
- [15] **LSST Project** Collaboration, P. A. Abell et al., *LSST Science Book, Version 2.0*, [[arXiv:0912.0201](#)].
- [16] LSST Dark Energy Science Collaboration, *Large Synoptic Survey Telescope: Dark Energy Science Collaboration, ArXiv e-prints* (Nov., 2012) [[arXiv:1211.0310](#)].
- [17] C. L. Carilli and S. Rawlings, *Science with the Square Kilometer Array: Motivation, key science projects, standards and assumptions*, *New Astron. Rev.* **48** (2004) 979, [[astro-ph/0409274](#)].
- [18] **Planck** Collaboration, P. A. R. Ade et al., *Planck 2015 results. XIII. Cosmological parameters*, *Astron. Astrophys.* **594** (2016) A13, [[arXiv:1502.01589](#)].
- [19] N. Palanque-Delabrouille et al., *Constraint on neutrino masses from SDSS-III/BOSS Ly α forest and other cosmological probes*, *JCAP* **1502** (2015), no. 02 045, [[arXiv:1410.7244](#)].
- [20] G. Drexlin, V. Hannen, S. Mertens, and C. Weinheimer, *Current direct neutrino mass experiments*, *Adv. High Energy Phys.* **2013** (2013) 293986, [[arXiv:1307.0101](#)].
- [21] J. Adamek, D. Daverio, R. Durrer, and M. Kunz, *General relativity and cosmic structure formation*, *Nature Phys.* **12** (2016) 346–349, [[arXiv:1509.01699](#)].
- [22] J. Adamek, R. Durrer, and M. Kunz, *N-body methods for relativistic cosmology*, *Class. Quant. Grav.* **31** (2014), no. 23 234006, [[arXiv:1408.3352](#)].
- [23] J. Adamek, D. Daverio, R. Durrer, and M. Kunz, *gevolution: a cosmological N-body code based on General Relativity*, *JCAP* **1607** (2016), no. 07 053, [[arXiv:1604.06065](#)].
- [24] J. Adamek, J. Brandbyge, C. Fidler, S. Hannestad, C. Rampf, and T. Tram, *The effect of early radiation in N-body simulations of cosmic structure formation*, *Mon. Not. Roy. Astron. Soc.* **470** (2017), no. 1 303–313, [[arXiv:1703.08585](#)].
- [25] I. A. Brown, J. Behrend, and K. A. Malik, *Gauges and Cosmological Backreaction*, *JCAP* **0911** (2009) 027, [[arXiv:0903.3264](#)].
- [26] D. Blas, J. Lesgourgues, and T. Tram, *The Cosmic Linear Anisotropy Solving System (CLASS) II: Approximation schemes*, *JCAP* **1107** (2011) 034, [[arXiv:1104.2933](#)].
- [27] J. Lesgourgues and T. Tram, *The Cosmic Linear Anisotropy Solving System (CLASS) IV: efficient implementation of non-cold relics*, *JCAP* **1109** (2011) 032, [[arXiv:1104.2935](#)].
- [28] J. Brandbyge and S. Hannestad, *Grid Based Linear Neutrino Perturbations in Cosmological N-body Simulations*, *JCAP* **0905** (2009) 002, [[arXiv:0812.3149](#)].
- [29] J. Brandbyge and S. Hannestad, *Resolving Cosmic Neutrino Structure: A Hybrid Neutrino N-body Scheme*, *JCAP* **1001** (2010) 021, [[arXiv:0908.1969](#)].
- [30] Y. Ali-Haïmoud and S. Bird, *An efficient implementation of massive neutrinos in non-linear structure formation simulations*, *Mon. Not. Roy. Astron. Soc.* **428** (2012) 3375–3389, [[arXiv:1209.0461](#)].

- [31] A. Banerjee and N. Dalal, *Simulating nonlinear cosmological structure formation with massive neutrinos*, *JCAP* **1611** (2016), no. 11 015, [[arXiv:1606.06167](#)].
- [32] M. Zennaro, J. Bel, F. Villaescusa-Navarro, C. Carbone, E. Sefusatti, and L. Guzzo, *Initial Conditions for Accurate N-Body Simulations of Massive Neutrino Cosmologies*, *Mon. Not. Roy. Astron. Soc.* **466** (2017) 3244, [[arXiv:1605.05283](#)].
- [33] C.-P. Ma and E. Bertschinger, *A Calculation of the full neutrino phase space in cold + hot dark matter models*, *Astrophys. J.* **429** (1994) 22, [[astro-ph/9308006](#)].
- [34] P. S. Behroozi, R. H. Wechsler, and H.-Y. Wu, *The Rockstar Phase-Space Temporal Halo Finder and the Velocity Offsets of Cluster Cores*, *Astrophys. J.* **762** (2013) 109, [[arXiv:1110.4372](#)].
- [35] J. Brandbyge, C. Rampf, T. Tram, F. Leclercq, C. Fidler, and S. Hannestad, *Cosmological N-body simulations including radiation perturbations*, *Mon. Not. Roy. Astron. Soc.* **466** (2017) L68–L72, [[arXiv:1610.04236](#)].
- [36] N. E. Chisari and M. Zaldarriaga, *Connection between Newtonian simulations and general relativity*, *Phys. Rev.* **D83** (2011) 123505, [[arXiv:1101.3555](#)]. [Erratum: *Phys. Rev.* **D84**, 089901(2011)].
- [37] S. R. Green and R. M. Wald, *Newtonian and Relativistic Cosmologies*, *Phys. Rev.* **D85** (2012) 063512, [[arXiv:1111.2997](#)].
- [38] S. F. Flender and D. J. Schwarz, *Newtonian versus relativistic cosmology*, *Phys. Rev.* **D86** (2012) 063527, [[arXiv:1207.2035](#)].
- [39] G. Rigopoulos and W. Valkenburg, *On the accuracy of N-body simulations at very large scales*, *Mon. Not. Roy. Astron. Soc.* **446** (2015) 677–682, [[arXiv:1308.0057](#)].
- [40] I. Milillo, D. Bertacca, M. Bruni, and A. Maselli, *Missing link: A nonlinear post-Friedmann framework for small and large scales*, *Phys. Rev.* **D92** (2015), no. 2 023519, [[arXiv:1502.02985](#)].
- [41] C. Fidler, C. Rampf, T. Tram, R. Crittenden, K. Koyama, and D. Wands, *General relativistic corrections to N-body simulations and the Zel’dovich approximation*, *Phys. Rev.* **D92** (2015), no. 12 123517, [[arXiv:1505.04756](#)].
- [42] C. Fidler, T. Tram, C. Rampf, R. Crittenden, K. Koyama, and D. Wands, *Relativistic Interpretation of Newtonian Simulations for Cosmic Structure Formation*, *JCAP* **1609** (2016), no. 09 031, [[arXiv:1606.05588](#)].
- [43] F. Villaescusa-Navarro, S. Bird, C. Peña-Garay, and M. Viel, *Non-linear evolution of the cosmic neutrino background*, *JCAP* **1303** (2013) 019, [[arXiv:1212.4855](#)].
- [44] D. Inman, J. Emberson, U.-L. Pen, A. Farchi, H.-R. Yu, and J. Harnois-Déraps, *Precision reconstruction of the cold dark matter-neutrino relative velocity from N-body simulations*, *Phys. Rev.* **D92** (2015), no. 2 023502, [[arXiv:1503.07480](#)].
- [45] E. Castorina, C. Carbone, J. Bel, E. Sefusatti, and K. Dolag, *DEMNUi: The clustering of large-scale structures in the presence of massive neutrinos*, *JCAP* **1507** (2015), no. 07 043, [[arXiv:1505.07148](#)].
- [46] J. D. Emberson et al., *Cosmological neutrino simulations at extreme scale*, *Res. Astron. Astrophys.* **17** (2017), no. 8 085, [[arXiv:1611.01545](#)].
- [47] V. Springel, *The Cosmological simulation code GADGET-2*, *Mon. Not. Roy. Astron. Soc.* **364** (2005) 1105–1134, [[astro-ph/0505010](#)].
- [48] J. Harnois-Déraps, U.-L. Pen, I. T. Iliev, H. Merz, J. D. Emberson, and V. Desjacques, *High Performance P3M N-body code: CUBEP3M*, *Mon. Not. Roy. Astron. Soc.* **436** (2013) 540, [[arXiv:1208.5098](#)].

- [49] M. Tegmark, A. J. S. Hamilton, M. A. Strauss, M. S. Vogeley, and A. S. Szalay, *Measuring the galaxy power spectrum with future redshift surveys*, *Astrophys. J.* **499** (1998) 555–576, [[astro-ph/9708020](#)].
- [50] R. Takahashi, M. Sato, T. Nishimichi, A. Taruya, and M. Oguri, *Revising the Halofit Model for the Nonlinear Matter Power Spectrum*, *Astrophys. J.* **761** (2012) 152, [[arXiv:1208.2701](#)].
- [51] S. Bird, M. Viel, and M. G. Haehnelt, *Massive Neutrinos and the Non-linear Matter Power Spectrum*, *Mon. Not. Roy. Astron. Soc.* **420** (2012) 2551–2561, [[arXiv:1109.4416](#)].
- [52] E. Lawrence, K. Heitmann, J. Kwan, A. Upadhye, D. Bingham, S. Habib, D. Higdon, A. Pope, H. Finkel, and N. Frontiere, *The Mira-Titan Universe II: Matter Power Spectrum Emulation*, [arXiv:1705.03388](#).
- [53] C. Wagner, L. Verde, and R. Jimenez, *Effects of the neutrino mass splitting on the non-linear matter power spectrum*, *Astrophys. J.* **752** (2012) L31, [[arXiv:1203.5342](#)].
- [54] G. Ballesteros, L. Hollenstein, R. K. Jain, and M. Kunz, *Nonlinear cosmological consistency relations and effective matter stresses*, *JCAP* **1205** (2012) 038, [[arXiv:1112.4837](#)].
- [55] G. Kulkarni, T. R. Choudhury, E. Puchwein, and M. G. Haehnelt, *Models of the cosmological 21 cm signal from the epoch of reionization calibrated with Ly α and CMB data*, *Mon. Not. Roy. Astron. Soc.* **463** (2016), no. 3 2583–2599, [[arXiv:1607.03891](#)].
- [56] D. Daverio, M. Hindmarsh, and N. Bevis, *Latfield2: A c++ library for classical lattice field theory*, [arXiv:1508.05610](#).
- [57] J. M. Sanz-Serna, *Symplectic integrators for hamiltonian problems: an overview*, *Acta Numerica* **1** (1992) 243–286.
- [58] T. H.-C. Lu, K. Ananda, C. Clarkson, and R. Maartens, *The cosmological background of vector modes*, *JCAP* **0902** (2009) 023, [[arXiv:0812.1349](#)].
- [59] D. Baumann, P. J. Steinhardt, K. Takahashi, and K. Ichiki, *Gravitational Wave Spectrum Induced by Primordial Scalar Perturbations*, *Phys. Rev.* **D76** (2007) 084019, [[hep-th/0703290](#)].